Effects of Free Stream Turbulence on Compressor Cascade Performance

Justin W. Douglas

Thesis submitted to the Faculty of the Virginia Polytechnic Institute and State University in partial fulfillment of the requirements for the degree of

Master of Science

In

Mechanical Engineering

Committee:

Dr. Wing Fai Ng, Chair

Dr. Clint Dancey

Dr. Thomas Diller

Dr. Shiming Li

March 1, 2001

Blacksburg, VA

Keywords: Turbulence Grid, Boundary Layer Transition, Aerodynamic Loss, Compressor Cascade, Hotwire, Anemometer

Effects of Free Stream Turbulence on Compressor Cascade Performance

Justin W. Douglas

(ABSTRACT)

The effects of grid generated free-stream turbulence on compressor cascade performance was measured experimentally in the Virginia Tech blow-down wind tunnel. The parameter of key interest was the behavior of the measured total pressure loss coefficient with and without generated free-stream turbulence. A staggered cascade of nine airfoils was tested at a range of Mach numbers between 0.59 and 0.88. The airfoils were tested at both the lowest loss level cascade angle and extreme positive and negative cascade angles about this condition. The cascade was tested in a Reynolds number range based on the chord length of approximately 1.2-2x10^6. A passive turbulent grid was used as the turbulence-generating device, it produced a turbulent intensity of approximately 1.6%. The total pressure loss coefficient was reduced by 11-56% at both the "lowest loss level" and more positive cascade angles for both high and low Mach numbers. Oil Visualization and blade static pressure measurements were performed in order to gain a qualitative understanding of the loss reduction mechanism. The results indicate that the effectiveness of an increasing turbulent free-stream on loss reduction, at transonic Mach numbers, depends on whether the shock wave on the suction surface is strong enough to completely separate the boundary layer. At negative cascade angles, increasing free-stream turbulence proved to have a negligible influence on the pressure loss coefficient. At cascade angles where transition exists within a laminar separation bubble, increasing free-stream turbulence suppressed the extent of the laminar separation bubble and led to an earlier turbulent reattachment.

ACKNOLEDGEMENTS

I would like to thank God for giving me the opportunity and the ability to obtain a Master's Degree. I would also like to thank Dr. Wing Ng for allowing me to conduct this research and for his patience and advice during a very trying project. Dr. Clint Dancey, Dr. Karen Thole, Dr. Joe Schetz, and Dr. Tom Diller, thank you for always allowing me to march into your offices with various questions at all hours of the day and night for advice on the subject of turbulence.

A special thanks to Dr. Shiming Li for all of the long hours of experiments in both successful and frustrating outcomes, you always showed great patience and encouragement. Your advice and guidance both on this project and the art of fishing have proved to be tremendously helpful. I would also like to thank Casey Carter, Bo Song, Todd Bailie, and Tom Vandeputte for their willingness to assist me with my experiments in any way that I needed. I would also like to thank Greg, Kurt, Bruce, Jamie, Bill, and Timmy, from both the AOE and ME machine shop for all of their valuable advice on machining issues. A special thanks to Dr. Michael Sexton for sparking the interests of a young cadet in the field of Turbomachinery, it inspired me to pursue this masters degree.

Finally, I would like to thank my fiancée, Marcia James, for supporting me both through the grueling years at the Virginia Military Institute and through Virginia Tech. For your love and support I am forever grateful. Special thanks to my parents, James Douglas and Jacqueline Crider for instilling in me that the only way to accomplish success is through hard work.

"...Times like these try men's souls." Thomas Paine

TABLE OF CONTENTS

TABLE OF FIGURES

INDEX OF TABLES

NOMENCLATURE

LE	Leading Edge of Stator
TE	Trailing Edge of Stator
SS	Suction Side of Stator
I	Cascade Angle, Degrees
Ms	Isentropic Mach Number
x/c	Percentage Chord
M1	Inlet Mach Number
M2	Exit Mach Number
Tt_1	Total Temperature, Upstream
Ts_1	Static Temperature, Upstream
Pt_1	Total Pressure, Upstream of Grid
Pt_{1cas}	Total Pressure, Upstream of Cascade, Downstream of Grid
Ps_1	Static Pressure, Upstream
Ps_2	Static Pressure, Downstream
Pt_2	Total Pressure, Downstream
dPt	Differential Total Pressure
Re	Reynolds Number Based on Chord
Tu	Turbulence Intensity
r	Density
g	Gamma=1.4, Cold-Air Standard
w	Pressure Loss Coefficient
m	Viscosity
a	Inlet Cascade Angle
b	Exit Metal Angle
C	Blade Chord, or Calibration Constant for HW Calibration
t	Pitch
x	Axial Distance

d diameter of bars in Turbulence Grid

M Mesh Size of Grid

R Gas Constant

U_1 Instantaneous Velocity, Upstream

U_{A2} Axial Velocity, Downstream

U_{A1} Axial Velocity, Upstream

AVDR-Axial Velocity Density Ratio

CDA Controlled Diffusion Airfoil

PVD Prescribed Velocity Distribution Airfoil

Chapter 1 INTRODUCTION

In today's ever-competitive gas turbine market, industry constantly strives for lower aerodynamic losses at both design and off design conditions. In the twenty-first century not only does industry feel pressure to lower losses to make their engines financially attractive, but also to meet the ever tightening emissions standards from the federal government. The efficiency of a gas turbine is largely dependent on its turbomachinery components. If engine designers are able to improve the flow efficiency through both the compressor and turbine side of the gas turbine, then less fuel must be added to obtain the higher levels of power that were once considered unsatisfactory due to emissions or industry standards for efficiency. Therefore, the design of blade profiles and the manipulation of the flow over these blade profiles in order to improve aerodynamic efficiency are of utmost importance. For example, when impingement cooling of turbine blades was introduced to industry the efficiency of the gas turbine cycle increased due to the capacity to run the turbine at higher inlet temperatures. The idea of fogging a compressor, or spraying water droplets into the inlet of an engine, in order to use evaporative cooling to achieve higher compression efficiency, is also being researched in this area.

The stators and rotors that make up the numerous stages of a compressor are designed to operate at a certain optimal condition, usually referred to as the design point. However, during their actual application they are operated at off design conditions as well. In these off design ranges the flow enters the stator and rotor stages at varying incidence angles, and lower losses are even more difficult to achieve due to certain flow phenomena such as flow separation and shock waves. These phenomena act to drive the losses to higher levels and eventually cause compressor

stall. Unlike turbines, the efficiency of a compressor is very sensitive to inlet incidence angle change due to the diffusing of the flow and the creation of an adverse pressure gradient. When the flow separates due to an adverse pressure gradient, the blade profile loss is dependent on the extent of the flow separation. The use of increased free-stream turbulence plays a role in manipulating this flow separation, and ultimately the performance of the compressor stage.

For years, researchers around the world have used cascade tests to conduct research and to push the envelope for running turbomachines at off design conditions. Although these cascade tests are not a perfect model representation of an actual rotating turbomachine, cascade testing provides the blade designer with a more economical and experimentally simpler method of examining the aerodynamic performance under various operating conditions. Cascade testing is also used for validation of computational fluid dynamic (CFD) flow solvers. These CFD programs are generally pretty accurate in predicting aerodynamic losses for subsonic flow unless flow phenomena such as shock waves or laminar separation are underestimated near transonic Mach numbers. Since new flow solvers are frequently being programmed and tweaked by industry, cascade testing is still a reliable method for determining the actual aerodynamic loss of a blade profile.

1.1 Background and Previous Research

Since cascade testing has evolved into an effective model for the testing of compressor blades, the parameters that control testing conditions have also changed over the years. It is common practice to find that wind tunnels around the country are designed for very low inlet turbulence levels. The advantage for designing a wind tunnel in this way is that it provides a good baseline for cascade experiments and presents the possibility to raise the turbulence level to a desired level in a controlled fashion. Now, common wind tunnel practice and actual gas turbine operation have raised the question of whether cascade testing without a suitable free-stream turbulence level is reliable, due to the turbulent rotor wakes internal to the engine. Gostelow (1984) believes that cascade results obtained without a suitable turbulence generating device are quite suspect.

1.1.1 Effects of Free-Stream Turbulence on Boundary Layer Transition

The generation of free-stream turbulence changes the characteristics of transition of the boundary layer on the suction surface of turbomachinery blades. Quantitatively, this transition point movement has been studied for years, but with the constant improvement of visualization techniques it is possible for these effects to be seen qualitatively. Work by Mayle (1991), Evans (1971), and Schreiber (2000) have extensively researched and eloquently documented the effects of turbulence on boundary layer transition.

Mayle (1991) gives a detailed description of the importance of understanding the role of boundary layer transition in a gas turbine. He defines four modes of transition characteristic to flow through the various stages of a gas turbine engine. The first mode is one of natural

transition, which begins with the formation of weak instabilities, or TS (Tollmien and Schlichting) waves, in the laminar boundary layer, followed by the development of larger instabilities, which eventually lead to fully turbulent flow. The second mode is called "bypass" transition and is characterized by the skipping of the TS instabilities with procession to fully turbulent flow. He points out that bypass transition is caused by large disturbances in the external flow, such as free stream turbulence. The turbulence spots that develop in the later stages of natural transition, just before fully turbulent flow, are present within the boundary layer without the TS wave procession and are caused by the large fluctuations impinged on the blade surface due to free-stream turbulence (Mayle,2001). The third mode of transition is one of locally separated laminar flow that is contained within a bubble, known as the laminar separation bubble. Mayle describes this transition as one that may occur in the free shear layer, like flow near the surface, and in this case the flow may reattach as a turbulent flow. He suggests that this type of transition can occur in an adverse pressure gradient, and that a method of making this bubble as short as possible is an effective control to improve performance. Lastly, he points out that for transonic airfoils wake-induced transition is observed and is characterized as periodic-unsteady transition. He summarizes this form of transition induced by wakes or trailing shocks from upstream rotors to be so disruptive to the laminar boundary layer that the turbulent spots form immediately and coalesce into a turbulent strip that grows as it propagates downstream.

The first three modes described above are easily understood in two dimensions, the fourth mode is completely a three dimensional effect, where more than one of the modes of transition can exist on the blade surface at one time, or multi-mode transition. Concerning strictly the notion of turbulence, Mayle made several distinct conclusions. First is that transition is dominated mainly

by the free-stream turbulence, pressure gradient, and the periodic unsteady passing of wakes. Second, onset of transition is significantly dependent upon free stream turbulence both intensity and scale. Next, he concludes that the effects of surface roughness, surface curvature, compressibility, and heat transfer on transition are secondary to those of free-stream turbulence. Lastly, the length of transition depends only on the turbulence level and the pressure gradient (Mayle,2000).

Evans (1971) studied the effects of turbulence on boundary layer transition in low-speed flow with Re ranging from 2-6x10^5, on compressor blades with a 12-inch chord. He tested these blades in turbulence levels up to 4%. Evans concludes that Reynolds number variation has little effect upon the position of laminar separation, but that the effect of generated free-stream turbulence causes a slightly earlier laminar separation or an earlier natural transition depending upon the Reynold's number. He notes that if the turbulence intensity is increased past the point where the laminar separation bubble is suppressed, then a natural attached transition will move toward the leading edge of the blade. Evans also finds that turbulence scale plays a role in how turbulence effects transition. He concludes that a given turbulence intensity with a small scale moves transition farther toward the leading edge of the blade than the same turbulence intensity with a larger scale. In the current work, the effect of scale was not studied due to time and positions available for the turbulence generator.

Schreiber (2000) conducted an investigation on the effect of Reynolds number and free-stream turbulence on boundary layer transition location on the suction surface of a controlled diffusion airfoil (CDA). The experiment was conducted in a rectilinear cascade at Reynold's numbers

ranging from 0.7-3.0x10^6 and turbulence intensities from 0.7 to 4%. Two flow visualization techniques were used in this experiment. For low speed tests oil visualization was used, but at high speeds the oil visualization was found to be less sensitive to skin friction discontinuities. In order to better visualize boundary layer phenomena at high Reynold's numbers, Schreiber used a liquid crystal technique that distinguishes differences in adiabatic wall temperatures. At small turbulence intensities (Tu<3%) and all Reynolds numbers tested, Schreiber finds that the accelerated front portion of the blade is laminar and that transition occurs within a laminar separation bubble shortly after the maximum velocity, which was found near 35-40% chord. Conversely, at turbulence higher than this range and high Reynold's numbers, Schreiber observes that transition propagates upstream into the accelerated front region of the blade. In this case Schreiber describes this moved transition mode at high Reynold's number and high turbulence level as a bypass mode, or one where the laminar separation bubble is not visible. Schreiber points out that testing between turbulence levels of 2-4%, transition onset location is most dependent on the Reynolds number. Schreiber concludes that surface roughness may also play a role in the movement of transition and should be examined in future research.

1.1.2 Effects of Incidence on Boundary Layer Transition and Separation

In order to examine the full background of the current research, it is important to look at all aspects that contribute to the development of boundary layers. The above authors have carried out very detailed investigations on the effects of turbulence on the characteristics of boundary layers, but stator incidence also plays a role in determining transition and separation of boundary layers. Work by Steinert (1994) has documented the effect of incidence on boundary layer behavior, and in turn, how this behavior influences the pressure loss coefficient for the given blade profile.

Steinert (1996) conducts a study using the liquid crystal visualization technique to examine transition, local separation, and complete separation at design and off-design of a controlled diffusion airfoil (CDA). The CDA's were designed for an inlet Mach number of 0.62, and with a total flow turning of 27.6^{o}. A total of seven blades were tested, with a chord of 70mm, and two blades instrumented with 10 static pressure taps on the suction and pressure sides of the blades, respectively. The chord Reynolds number at design was $8x10^{5}$ and the free-stream turbulence level was 2.5%. It should be noted, that all tests conducted were with a constant turbulence level so the effects of varying turbulence level at different incidence angles is not represented in his work. However, assuming the turbulence level in Schreiber's work as a baseline, valuable boundary layer behavior and loss coefficient trends can be observed from his experiments. Steinert describes the importance of surveying the whole blade surface and not only point-by-point measurements, because both transition and separation are three-dimensional even in a linear cascade.

Steinert first examines the effect of incidence on boundary layer transition at constant inlet Mach number. Steinert reported that a range of plus or minus 4^{o} incidence of the design point that the boundary layer behavior on the suction side of the airfoil was almost identical with a laminar separation bubble at about 42-51% chord with turbulent reattachment. He notes at negative incidences that the separation bubble moves slightly downstream. At the incident angle of about plus 5^{o}, the laminar separation bubble vanished and transition moved to about 22% chord with complete separation at about 60% chord. An additional increase in incidence of one degree, shows that transition moves to 10% chord and then separates at about 50-55% chord. He describes this transition as somewhat unsteady, so the author assumes this is a bypass transition

mode. On the pressure side Steinert reports that transition occurred at around 20-23% chord, except at extreme negative incidence a small separation bubble was observed around 3% chord due to a shock wave caused by the expansion around the leading edge of the airfoil. Steinert's most interesting findings were when the inlet Mach number was varied and a loss profile was given as a function of inlet Mach number for design, positive, and negative incidence. At design, he describes the boundary layer transition to consist within a laminar separation bubble at around 40-50% chord with turbulent reattachment up to an inlet Mach number of 0.79. At transonic Mach numbers above this point, he reports a slight movement forward of the transition point followed by complete laminar separation. He concludes that this separation is probably caused by a lambda shock system interacting with the boundary layer, that in turn, results in complete separation. He supports this theory with the calculation of the respective supersonic isentropic Mach numbers on the blade surface in the accelerated front portion of the airfoil. At transonic Mach numbers he documents a steep increase in the loss coefficient. At negative incidence he notices that this choking and separation of the boundary layer first appears at an inlet Mach number of 0.626. At positive incidence of higher than plus 4^{o}, he described the cascade as again being in a choked state and with increasing inlet Mach number the losses increase very sharply as the flow is completely separated. Steinert mentions in conclusion that the Axial Velocity Density Ratio (AVDR), has a common inversely proportional effect on the loss coefficient. This may be better explained as the tendency of losses to decrease with increasing AVDR and flow turning. The AVDR may also be defined as a measure of the two-dimensionality of the flow. The AVDR is varied between 0.98 and 1.15 in Steinert's research.

1.1.3 The Effect of Free-Stream Turbulence on the Loss Coefficient

The final perspective in studying the background for the present work is to examine previous literature for documentation of the direct effect of free-stream turbulence on the calculated pressure-loss coefficient through a compressor cascade. Finding a substantial amount of relevant work that documents the direct effect of turbulence on the loss coefficient is somewhat difficult, work by Evans (1985) and Citavy (1977) provide some direct insight to this phenomena.

Evans (1985) performed boundary layer, pressure loss, skin friction, and deviation angle measurements in the presence of varying free stream turbulence on a cascade of compressor blades that had a 1 foot measured chord. The experiments were conducted in turbulent free streams at intensities of 0.68%, 3.14%, and 5.2%, and a constant Reynolds number of $5x10^5$. The angle of attack tested was at plus 4^o of the design incidence. The blades were designed for 43.35^o total turning, and a solidity ratio of 0.709. Agreeing with other researchers' results, Evans found that at increased turbulence levels the laminar separation bubble will shorten, and eventually collapse. Even higher turbulence levels caused the transition point to move towards the leading edge of the blade (Evans,1985). Evans conducted boundary layer measurements at 30%, 50%, 70%, and 80% chord on the suction surface of the blade to observe the characteristics of the boundary layer under varying degrees of turbulence. Evans found that with increasing turbulence the momentum thickness decreased, which in turn, signifies an increasing velocity profile thickness. At chord-wise locations close to the separation point momentum thickness tends to increase with increasing turbulence below 3%. At turbulence levels above 3% the effect of an increased velocity profile fullness again becomes dominant even near separation and momentum thickness again tends to decrease. Evans reports that at all values of the adverse

pressure gradient, skin friction is seen to increase with increasing free-stream turbulence, which he notes is consistent with the increased fullness of the velocity profiles. Evans observes two distinct characteristics of the pressure loss coefficient during his experiments. First, when turbulence levels are between 0.68-3%, he documents a slight increase in the pressure loss coefficient. He explains that this is due to the thickening of the boundary layer and an increase the momentum thickness. At turbulence levels higher than 3%, he records a drop in the pressure loss coefficient. He explains this increase in performance as the increase of turbulent energy content of the boundary layer caused by an increased entrainment of the turbulent free-stream. This increased energy means that the boundary layer can sustain a larger adverse pressure gradient near the trailing edge before separation. Evans proves this theory by measuring the deviation angle at increasing turbulence levels, and reports that with increasing turbulence levels the deviation angle decreases. This signifies a boundary layer that stays attached to the blade surface over a greater portion of the blade.

Citavy (1977) performed experiments on prescribed velocity distribution (PVD) compressor blades in a Reynolds number range of $0.6x10^5$ to $2x10^5$ to document the effects of free stream turbulence and Reynolds number on cascade performance. Although the author acknowledges that the research of Citavy may be at Reynolds number level too low for direct comparison to the current work, the trend that Citavy documents from his experiments are completely relevant. Citavy reports that at increasing turbulence levels that the laminar separation bubble length is reduced and that this realizes a significant reduction in pressure losses and small decrease differences in the outlet flow angle at all Reynolds numbers tested. It is of interest that as Citavy lowers the Reynolds number, that a point exists where the separation bubble bursts and complete

separation with reattachment is observed. The influence of free-stream turbulence lowers this bursting Reynolds number significantly from his baseline testing. It is also apparent at these Reynolds numbers close to the bursting state, that the outlet flow angle is most sensitive to free-stream turbulence.

1.2 Objective of the Current Work

The current work hopes to attempt to bring most of the previous research together and examines the effects of free-stream turbulence on the pressure loss coefficient at varying degrees of incidence and varying inlet Mach numbers. Once this effect is determined quantitatively, in terms of the calculated pressure loss coefficient, then the author would like to try and explain these effects somewhat qualitatively by the use of oil visualization and static pressure data obtained from the respective suction and pressure sides of the airfoil. The current work compares data from a baseline case, with low levels of free-stream turbulence, to that of a turbulence-generated free-stream. All inlet conditions were held constant between the two phases of the experiment to provide a detailed effect, if any, of free stream turbulence on the performance of the compressor cascade. In conclusion, the author will compare the experimental results with that of previous literature to analyze, reinforce, and discuss the validity of these results.

Chapter 2 EXPERIMENTAL METHOD

The following chapter is a description of the experimental setup in the laboratory. Section 2.1 describes the cascade design and capability. Section 2.2 gives a detailed description of the design of the turbulence grids. Section 2.3 describes the wind tunnel facility. Section 2.4 describes the instrumentation and data acquisition techniques used in the current experiment. Section 2.5 describes the flow visualization techniques used for baseline testing, while 2.6 describe the data reduction procedures and techniques.

2.1 Description of Cascade

The test section used for this research consisted of a nine-blade, 2-D, linear, compressor stator cascade contained within two Plexiglas sidewalls. This set-up formed eight complete passages, however, only the two middle passages were used for the recording and documentation of data. The cascade can be tested at a 24 ^{o} inlet cascade angle range, a_1. The stators are designed to be used in a gas turbine engine. Table 2.1 summarizes the geometric properties of the compressor cascade. Figure 2.1 and Figure 2.2, show a schematic of the turning on each blade, and a picture of the assembled cascade, respectively.

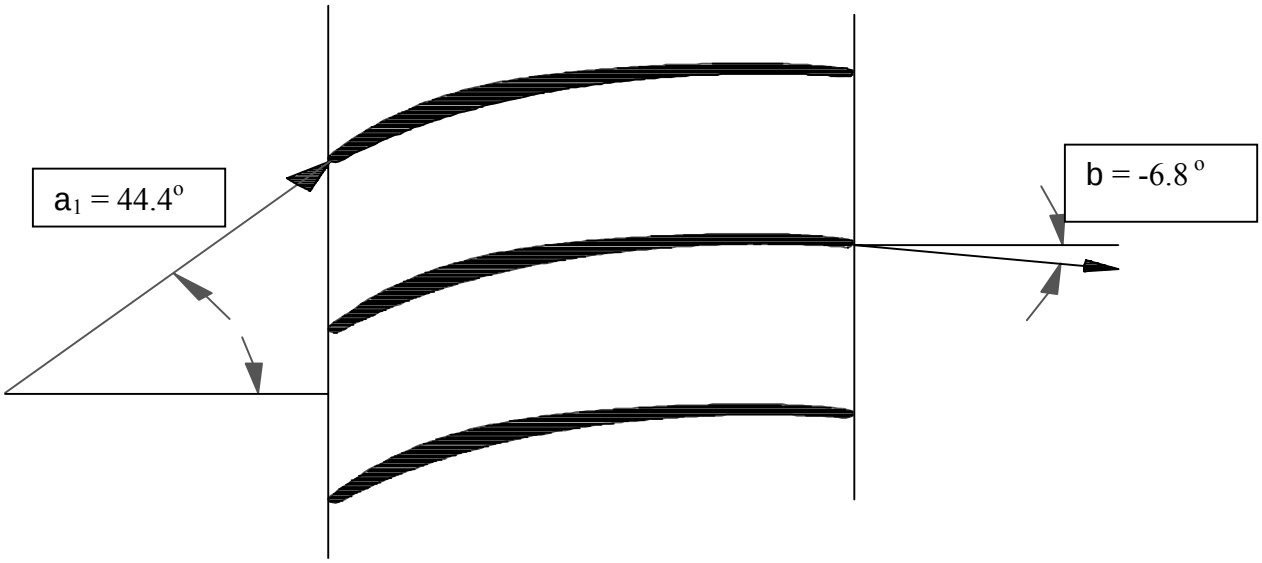

Figure 2. 1 Schematic of Stator Geometry

Table 2. 1 Blade Specifications, Minimum Loss Condition

Blade Chord, C	3.39 inches
Pitch, t	1.69 inches
Span	6 inches
Solidity	2.00
Inlet Cascade Angle, a_1	44.4^o
Exit Metal Angle, b	-6.8^o

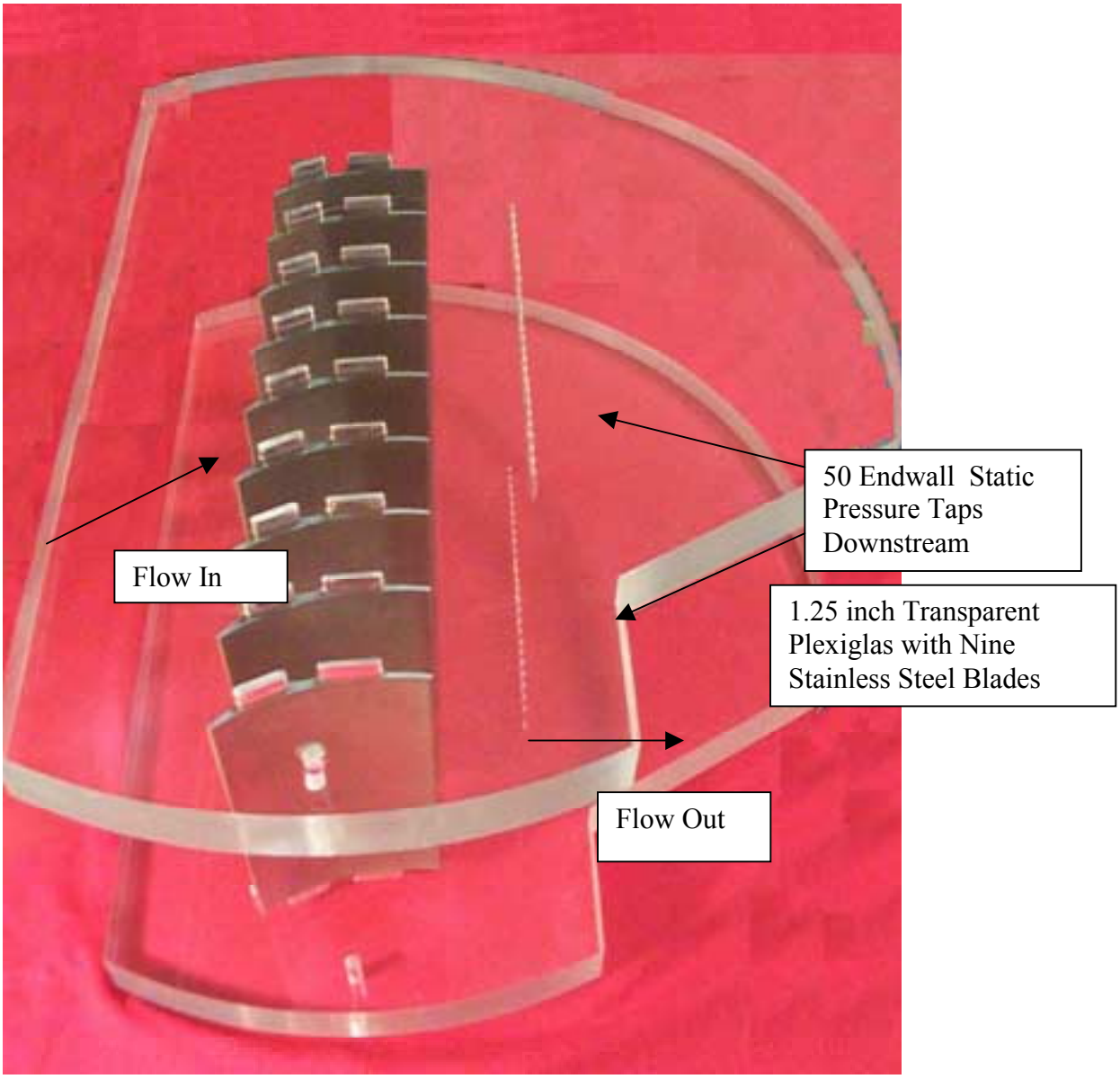

Figure 2. 2 Assembled Compressor Cascade

Figure 2.2 shows only the baseline-testing configuration, while Figure 2.8 shows the assembled cascade for testing with an upstream angle probe and hotwire probe at different pitchwise locations. The blades were electrical discharge machined (EDM) from 304 Grade Stainless Steel stock.

2.2 Description of Turbulence Grid Design

This chapter describes all aspects of the design, position, and implementation of the turbulent grid used in this experiment. It should be noted that two turbulent grids were designed and tested, however due to a nonuniform upstream flow with the first iteration the results were unreliable and the results discarded. The purpose of designing and implementing a turbulent grid was to increase the free stream turbulence of the flow entering the cascade. Increasing this turbulence level was hoped to lower the aerodynamic losses through the cascade by suppressing or moving boundary layer transition closer to the leading edge of the stator. This movement or suppression should force the flow to stay attached longer, thus increasing the aerodynamic performance.

2.2.1 Turbulence Decay Model

According to normal grid theory for a round bar, square mesh grid (Roach, 1987), turbulence intensity is given as

$$Tu = 0.80\left(x/d\right)^{\frac{-5}{7}}$$ **Equation 2. 1 (Roach,1987)**

$$Tu = 1.12\left(x/d\right)^{\frac{-5}{7}}$$ **Equation 2. 2 (Baines,1951)**

where d, is the bar diameter and x, is the axial distance. Equation 2.2 was used as the primary decay model for the design of the turbulence grid used in this experiment. This relationship is commonly known as the –5/7 Power Law. Roach gives some important restrictions on the use of Equation 2.1 such as:

(1) The above equations are limited to the isotropic, or well developed region, approximately 5 to 10 grid dimensions (mesh width) downstream of the grid (Baines,1951)

(2) The inlet flow to the grid consist of a low turbulence level

(3) Grid must be normal to the flow

(4) The test section should be significantly large compare with the grid mesh width to avoid sidewall boundary layer distortion

The notion of isotropic turbulence is that of developed turbulence that is unaffected by any external force will only change according to its own decay. Turbulent flow fields that are examined both near a wall and close to the turbulent source are not valid isotropic regions. These flow fields are commonly referred to as anisotropic regions. Isotropic turbulence is maintained by the energy cascade where larger eddies break up into smaller eddies and so on until the smallest eddies are viscously dissipated (Holmberg,1996). The turbulence measurements in this work were conducted 11.5 mesh widths, downstream of the turbulence grid and at midspan of the test section. The baseline turbulence intensity to the entrance of the grid in this experiment was measured to be approximately 0.1%. In this work the turbulence grid is placed normal to the upstream flow and its position in the wind tunnel will be discussed in further detail in Section 2.2.3. The size of the test section used for this work is 4.5 grid dimensions, which is relatively small and therefore did not follow this theory as precisely as expected.

2.2.2 Sizing of Bars and Mesh

Figure 2.3 shows a photograph of the turbulence grid used in this experiment, while Figure 2.4 shows a dimensioned schematic of the grid. The grid was designed in the form of a metal gasket

so that it could be easily swapped in and out of our tunnel without much disassembly or loss of time. The plate and circular bars are both fabricated from common 1040 cold rolled steel stock. The metal plate is 5/8 inch and the bars are 7/16 inch in diameter. In order to accommodate the 1/8 inch overhang of the bars on each side of the plate, they were milled down to 5/16 inch and then welded into the plate. The bead formed by the weld was then grinded down flush with the plate. Since the surface around the perimeter of the lattice of the grid is now smooth, a 1/16 inch black rubber gasket was inserted on both sides of the grid to ensure a good seal. Figure 2.3 shows a photograph of the turbulence grid. It should be noted that on the reverse side of the intersection of the bars the weld is not exposed to the flow in a way that would disrupt the wake of the bar and the formation of turbulence. Figure 2.4 shows a schematic of the turbulence grid so that the reader may get an idea of the general dimensions of the turbulence grid.

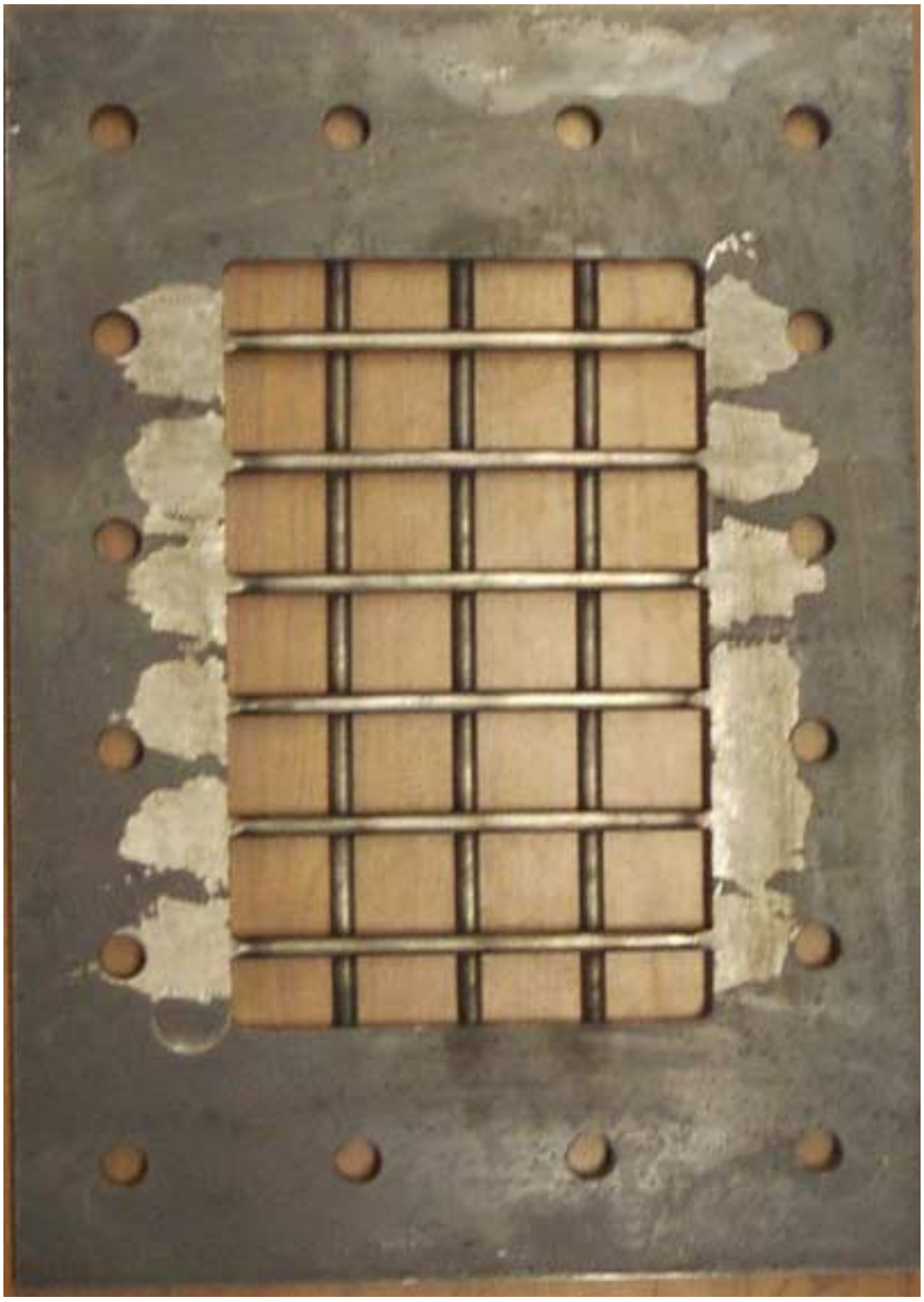

Figure 2. 3 Photograph of Turbulent Grid

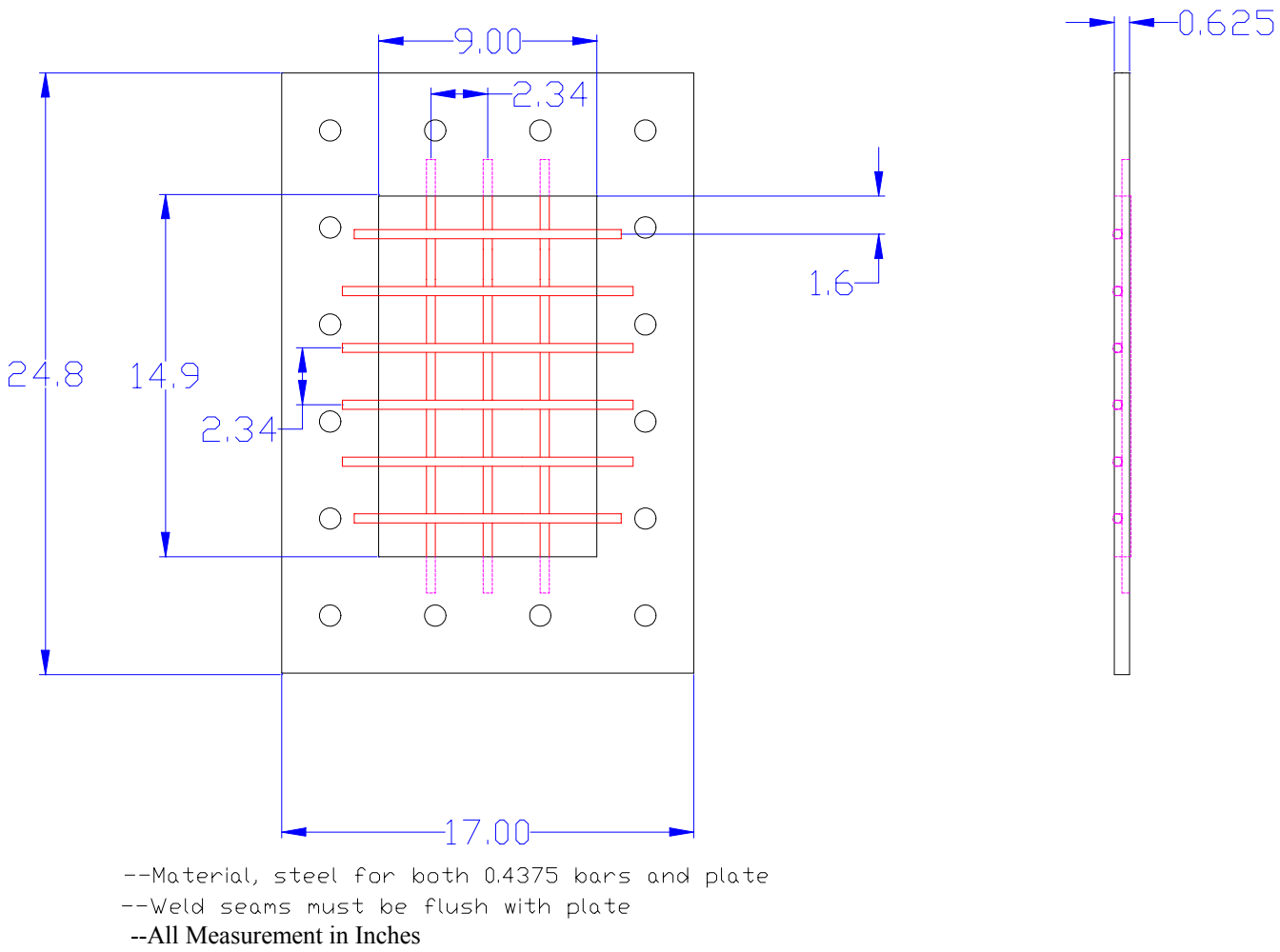

Figure 2. 4 Schematic of Turbulence Grid

The diameter of the bars were sized according to the –5/7 Power Law, the axial distance to the leading edge of the stators, and the turbulence intensity. Roach's –5/7 Power Law was used in the actual design of the grid because its lower coefficent of 0.80 predicted the turbulence intensity as a worst case scenario. However, after the diameter of the bars were designed using this relationship, this diameter was then substituted into Baines's Power Law equation in order to use Baines' experimental data presented graphically to design the mesh width between the bars. Baines (1951) points out that in the region of isotropic turbulence decay it is the bar size *b* rather

than the mesh size *M* that is the significant reference length. The mesh size used in the design of the turbulence grid for this work was one that was chosen to be operable based on the the work of Baines (1951), while the bar diameter was held as the design priority. The bars used in this study were designed based on a turbulence intensity of 4.5% and due to Schreiber's (2000) discussion on boundary layer transition propagation. Schreiber explains that about 4-5% turbulence intensity the boundary layer transition point propagates upstream to the front 10% chord of the studied compressor blade. A detailed discussion and analysis of the measured turbulence intensity and its effects on the flow will be included in Chapter 3 of this work.

2.2.3 Position of Turbulence Grid

Figure 2.5 shows the location of the turbulence grid within the test section and will allow the reader to establish a reference to the compressor cascade.

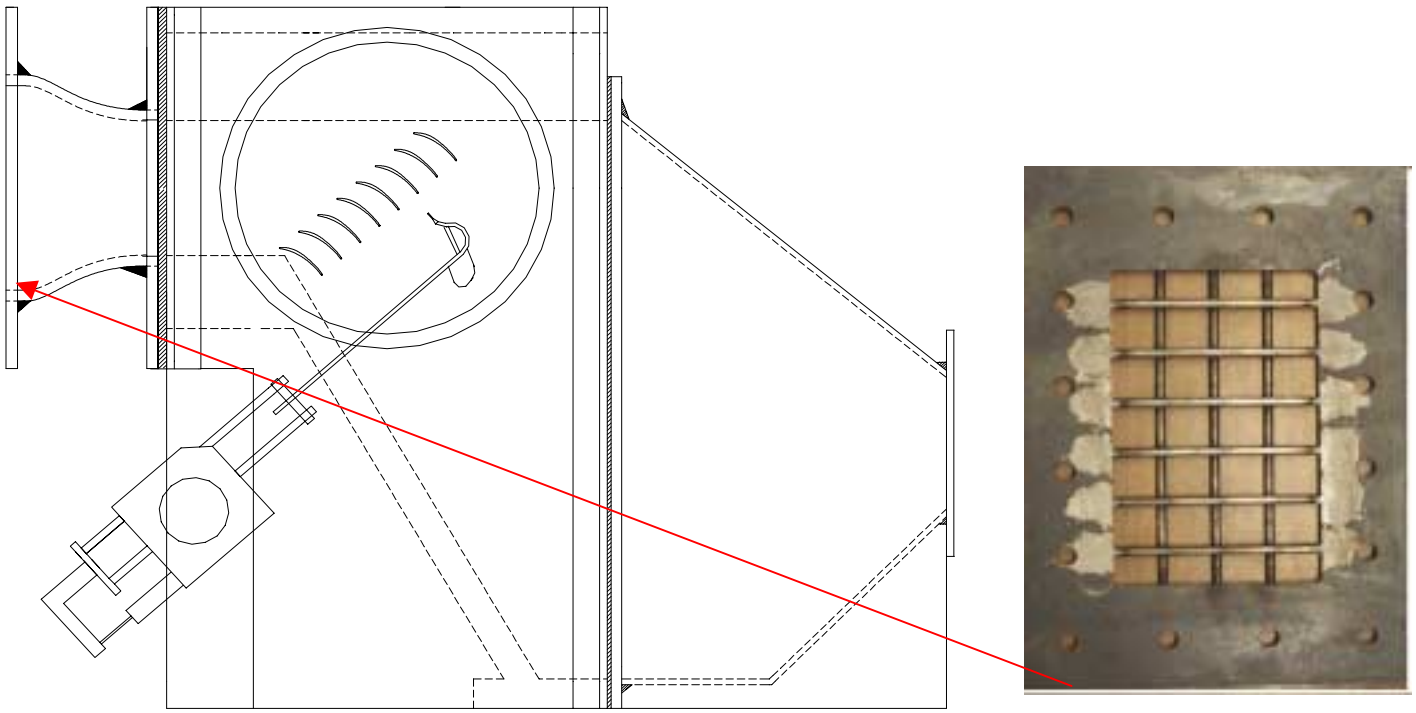

Figure 2. 5 Position of Turbulence Grid

The centerline of the turbulence grid is 23 inches from the middle passage of the compressor cascade. The reader may find it interesting that the grid is placed normal to a staggered cascade due to previous studies with free stream turbulence generation the turbulence grid and cascade are staggered at the same angle. However, due to the axial distance separating the grid and the cascade, and the prediction of the turbulence decay used for this study, it was realistic to place the grid normal to the staggered cascade. Since the grid was designed for an axial distance of 23 inches from the cascade, the turbulence decay is in its asymptotic decay region, so that an axial distance within plus or minus four or five inches would be proportional to a negligible decay. In other words, even though the cascade is staggered, each stator will see approximately the same turbulence level.

2.2.4 Prediction of Wake Width and Mixing Point

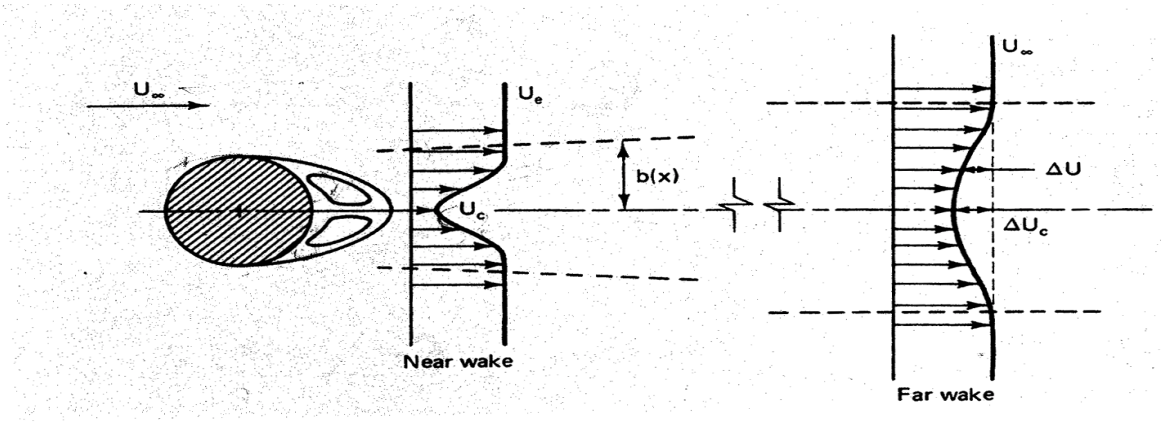

Figure 2. 6 Wake from Single Bar (Schetz,1993)

Figure 2.6 (Schetz, 1993) shows a schematic of the variables examined in the prediction of a wake from a single bar. The prediction of bar wake diffusion and the point where the wakes begin to mix were very important in this work. It is important because if the wakes are detected in the downstream pressure loss measurements the results could be confusing or misinterpreted.

In the first design iteration of the turbulence grid, the detection of the wakes of the bars just upstream of the cascade, caused the downstream flow to be very aperiodic and thus the results were unreliable. Wake flows from bars are made up of two regions, the near wake, right behind the body, and the far wake. The near wake is complicated and often involves separated flows and was not of interest for the design of the turbulent grid in this work (Schetz,1993). The point of interest in this work was the momentum deficit, or far wake profile, at the axial distance separating the turbulence grid with the leading edge of the stator passages to be examined. The following equations were used to calculate the variables shown schematically in Figure 2.7 (Schetz,1993).

$$b(x) = 0.57 \cdot \left(x \cdot C_D \cdot D\right)^{\frac{1}{2}}$$

Equation 2. 3 (Schetz,1993)

$$\frac{\Delta U_C}{U_\infty} = 0.98 \cdot \left(\frac{C_D \cdot D}{x} \right)^{\frac{1}{2}}$$

Equation 2. 4 (Schetz,1993)

Where x is axial distance, C_D, is the coefficient of drag, D, is the cylinder diameter, and U, is velocity both at the centerline of the cylinder and free-stream, respectively. Equation 2.3 calculates what the width of the wake, b(x), at some axial distance x. This distance is measured from the centerline of the blunt body, in this case a circular bar. When this analysis of one bar was coupled with the other bars in the grid, separated by a mesh dimension of approximately 2 inches, the mixing point of the span-wise and pitch-wise bars could be predicted. It may be easy for the reader to visualize the mixing from the horizontal bars and where the wake mixing point will be located, however, the vertical bars are more challenging to visualize. It should be noted that both the horizontal and vertical bars will have the same mixing point three dimensionally if

the mesh width is equal and symmetric throughout the grid. It was a priority to the design and placement of the turbulent grid to know where this mixing point occurred and ensure that it was a upstream of the cascade as soon as possible. Equation 2.4 predicts the momentum deficit in the far wake profile. The closer the velocity ratio in Equation 2.4 is to unity, the more uniform the upstream flow to the cascade becomes. The design of the turbulence grid ensured that the mixing point was predicted to be as far upstream as possible to allow the bar wakes to have an adequate mixing distance before entering the cascade. The author did not attempt to numerically predict the momentum deficit in the mixing region upstream of the cascade. This momentum deficit was determine experimentally by an upstream total pressure traverse performed at the leading edge of the stators to be examined. The total pressure traverse proved to be uniform, signifying that the wakes of the bars had sufficiently mixed. The total pressure traverse is shown in Figure 2.7.

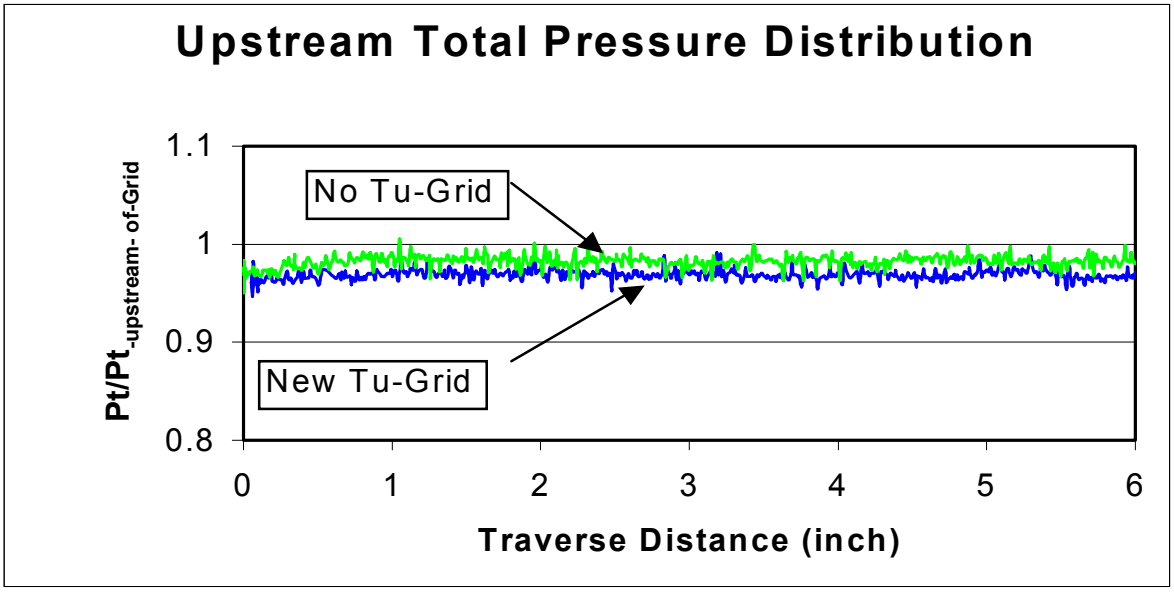

Figure 2. 7 Upstream Total Pressure Traverse

Figure 2.7 shows the total pressure measured at the leading edge of the middle cascade stator, normalized by the total pressure upstream of the turbulence grid. The reader may expect a larger pressure drop across the turbulence grid due to it size and blockage; however, since the grid is located upstream of the convergent nozzle to the test section the velocity is relatively low.

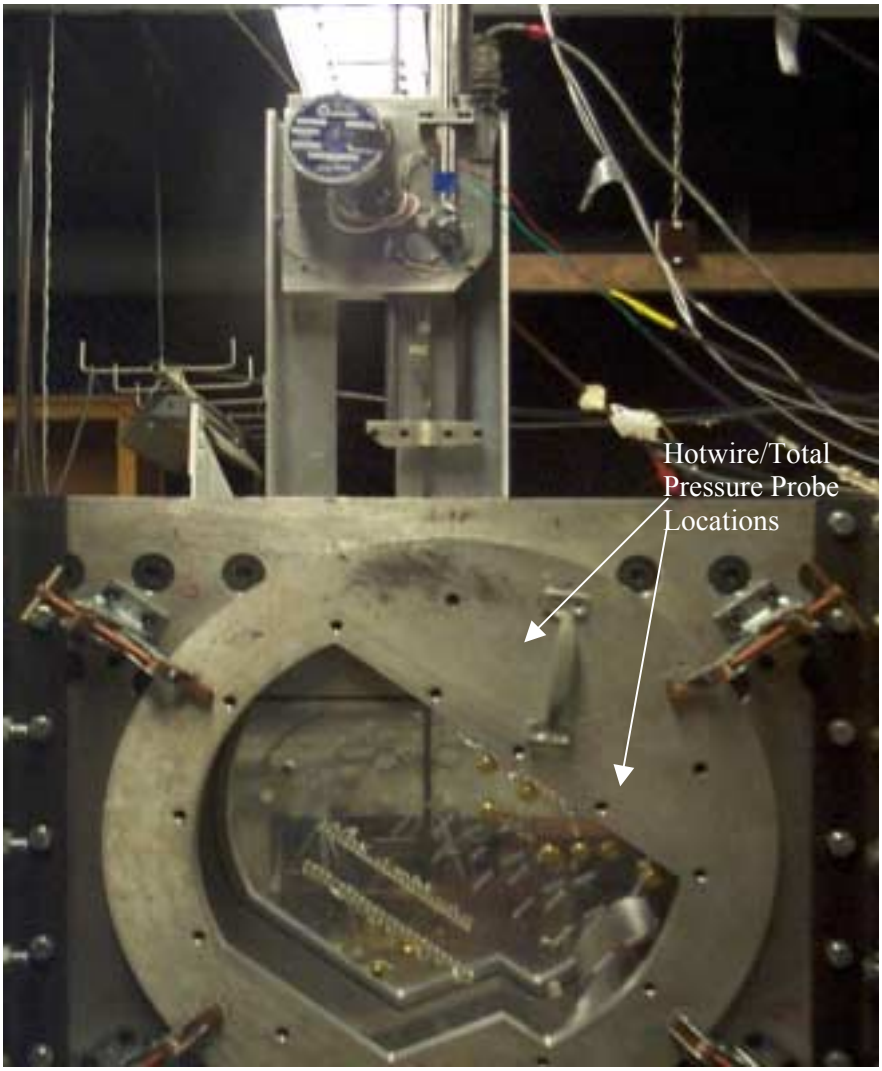

Figure 2. 8 Upstream Traverse Assembly

2.3 The Wind Tunnel Facility

The compressor cascade was tested in the transonic wind tunnel at Virginia Tech. The transonic wind tunnel is a blow-down type of facility. The supply air is stored in two large storage located on the outside of the laboratory and is pressurized by a four stage, reciprocating compressor. A power control panel on the inside of the laboratory is used for control of the loading, unloading, and activation of the blow-down sequence. Upon discharge from the storage tanks, the air is cooled and passed through an activated-alumina dryer to dehumidify the air before entering the wind tunnel. Although the dryer works to dehumidify the supply air, it is also necessary to drain the condensation due to ambient air compression from each stage of the compressor every 10-12 consecutive tunnel runs. A pneumatically controlled butterfly-type control valve is fed by pressurized reference air at 20psig and 80psig control air, and is used to maintain a constant inlet total pressure to the test section. A personal computer is used to supply a voltage signal to an electro-pneumatic converter that produces a proportionate output pressure based on the input voltage from the computer. The voltage signal from the computer is described by seven constants, among those constants is the inlet objective total pressure. The inlet objective total pressure is varied to produce a range of different inlet Mach numbers to the test section. Essentially, the tunnel computer uses feedback from the upstream total pressure probe to maintain constant total pressure in the test section. After the air passes through the control valve, it proceeds through a flow straightener and a meshed wire frame to provide uniform flow to the test section. This meshed wire frame is located far enough upstream so that any turbulence produced has decayed to an isotopic state and has an intensity of 0.1%. Typically, the valve takes 5 seconds to attain steady inlet total pressure and then is able to sustain this pressure for up to 15 seconds. Figure 2.9 shows a schematic of Virginia Tech's blow-down wind tunnel facility.

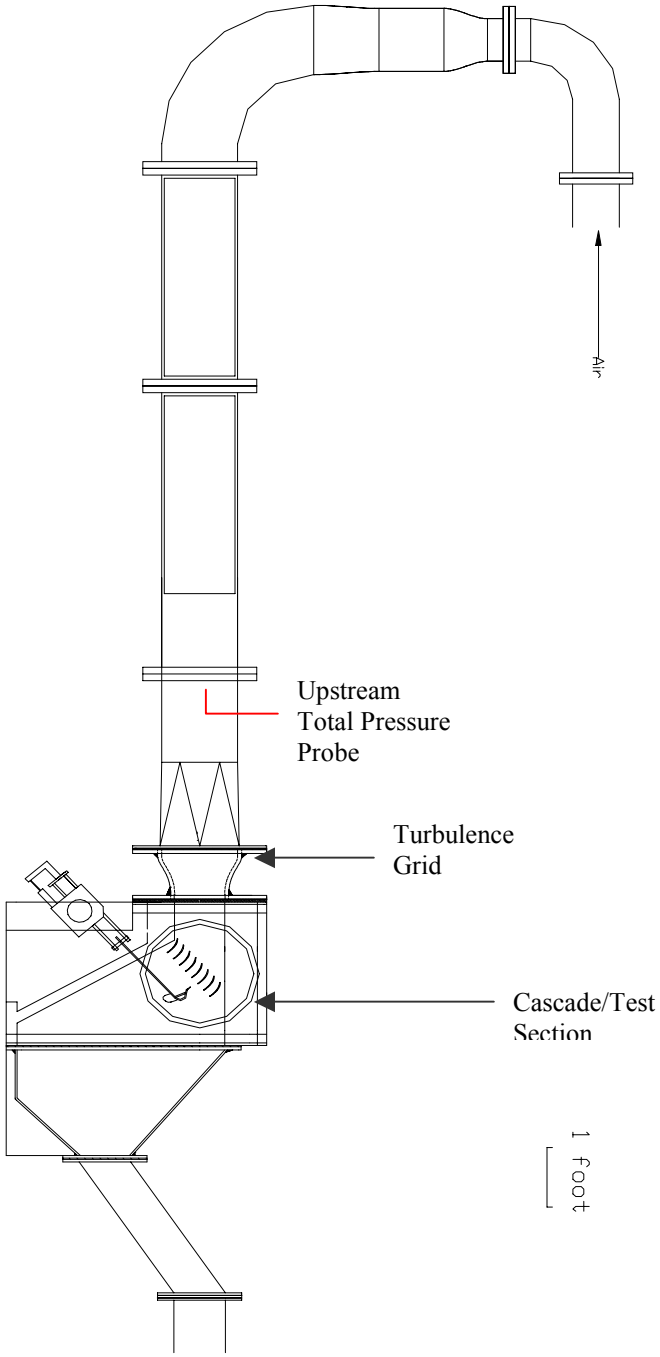

Figure 2. 9 Virginia Tech Transonic Wind Tunnel

The test section is fabricated with an aluminum frame with openings on each side for the installation of the compressor cascade. The top and bottom aluminum blocks of the test section form the top and bottom of the test section. The top and bottom blocks each have 0^o entry and 51^o, 60^o exit angles, respectively. Plexiglas, 1.25 inches thick, encloses the compressor stator on each side and make up the side wall of the flow region. The Plexiglas is held in place with 5 brass screw clamps on each side and a 12 inch C-clamp on top. The clamps support the test section in a way that the compressor stators are visible from both sides of the assembled test section. This visibility allows for optics-based flow visualization. The assembled Plexiglas cascade is able to rotate freely inside of the aluminum test section so that a range of flow incidence angles may be tested. The bottom block of the test section houses a smaller removable block that allows the experimenter to insert a downstream probe for traversing the downstream flow conditions. In this study, the removable block allowed for measurements at 50% chord downstream of the trailing edge of the stators. The removable block was fabricated with 5 distinct probe holes that were machined at different angles so that when the cascade was tested at off design angles the probe location would still maintain a traversing distance of 50% chord downstream of the cascade. The unused probe locations were sealed with Allen screws when not in use. The block allowed for an inlet incidence angle range of plus or minus 12^o from design.

2.4 Description of Instrumentation and Data Acquisition

This section describes the instrumentation involved in examination of aerodynamic losses, turbulence intensity, and location of suction and pressure side flow separation.

2.4.1 Upstream and Downstream Total and Static Pressure Measurements

Aerodynamic measurements were conducted to investigate the variation of losses at various design and off design incidence angles. These investigations were made with and without grid generated free-stream turbulence. Aerodynamic measurements used for calculating losses included:

- Upstream total pressure
- Upstream static pressure
- Differential total pressure between upstream and downstream conditions

In the experiments conducted at baseline conditions, or no turbulence generation, the upstream total pressure, Pt_1, was measured with a stationary Pitot probe positioned approximately 3.5 feet upstream of the test section. This Pitot probe was connected to a pressure transducer capable of measuring from 0 to 15 psig. During testing with grid generated turbulence the upstream total pressure, Pt_{1cas}, was measured with a stationary Pitot Probe approximately 4 inches upstream of the cascade and about 1 inch from the sidewall. The diameter of this pitot probe was 1/8 inch in diameter to avoid any shock losses introduced into the cascade due to its blunt body. In previous research in Virginia Tech's transonic wind tunnel, the sidewall boundary layer was measured to be no more than 0.25 inches so that 1 inch spanwise location of this probe is reliable. This Pitot

probe was connected to a pressure transducer capable of measuring pressure from 0 to 15 psig. The pressure transducer's used for all stagnation pressure measurements were located in a pressure transducer box that had the capacity for 13 simultaneous pressure measurements and a various range of pressure limits from 0 to 30 psig. The pressure transducers were calibrated using a variety of calibrating devices such as: an AMETEK deadweight tester, Fluke pressure calibrator, and a Venturi tube with an MKS pressure transducer. With each of the calibrating devices a known pressure was input to obtain a voltage reading from the output of the transducer being calibrated. In every case, each transducer was calibrated in 1-psig increments for the full psig rating of the respective transducer. The calibration of these transducer's proved to be very critical in trying to measure aerodynamic losses because when a transducer was not calibrated very meticulously error was introduced in the data reduction and made repeatability very difficult to achieve.

Upstream and downstream static pressure, Ps_1 and Ps_2, were measured with static taps through the Plexiglas sidewalls of the cascade. The sidewall static pressure taps are labeled in Figure 2.2. All static pressure taps were 1/32 inch in diameter and measured pitchwise static pressure. There were a total of 10 upstream static taps and 50 downstream static pressure taps. The upstream static pressure taps surveyed the middle two passages of the cascade, while the downstream static pressure taps measured the middle four passages of the cascade. The upstream static taps were located at 43% chord in the streamwise direction before the leading edge of the stators and were fabricated at the same stagger angle of the cascade. This was done so that all static pressure measurements were taken equidistant from each stator and far enough upstream to avoid any potential flow effects from the blades. The upstream static taps were spaced at a distance

25% pitch apart. The downstream static taps where located at 50% chord in the streamwise direction away from the trailing edge of the stators and spaced 17% pitch apart.

The static pressures were recorded using an independent, self-calibrating Pressure Systems Incorporated (PSI) Model 780C pressure scanning system. The PSI is controlled by a personal computer and has the capacity to read 64 channels from the pressure scanner. The PSI math processor processes the voltage signals returned by the pressure scanner, and pressure data is written to the control computer directly in gage pressure. For this experiment, the PSI was set to scan the static pressures for 15 seconds. During this time, the PSI records 14 static pressures, each of which was an average of ten measurements from each sidewall static pressure tap. The PSI system used a 0 psig vacuum pressure and a 100 psig positive pressure to automatically calibrate its scanner before each run. The 100 psig pressure was supplied from a compressed air tank, while the vacuum pressure was sustained using a small external vacuum pump. In the latter part of this work the upstream and downstream static pressures were recorded with pressure transducers at the top and bottom of the passages examined and then averaged due to technical problems with the PSI system.

The differential total pressure, dPt, or Pt1-Pt2, of upstream and downstream conditions was measured and recorded using a single differential pressure transducer. The upstream total pressure mentioned above was connected to the positive side of a pressure transducer using a piping tee, while the downstream total pressure was connected to the negative side of the transducer, providing the recorded pressure difference. The differential pressure transducer used to measure this pressure difference had limits of 0 to 15 psig. The downstream total pressure

was measured using a 3-hole total pressure traversing probe with static pressure measuring capability. The probe tip was angled through the previously described holding block to exactly match the exit angle of the blade. The probe traveled in the pitchwise direction parallel to the exit plane of the compressor cascade. The tip of the probe was located in the same streamwise location as the downstream static pressure taps, 50% chord. The static pressure measured by the probe provided a convenient check of the free stream static pressure and the sidewall static, which were found to be in very good agreement. The traversing probe's movement was controlled using a Rapidsyn stepper motor. The motor was in turn controlled by a personal computer that was programmed to traverse a specified linear distance with a specified velocity. In this study the probe traverse was programmed to traverse the middle two passages of the cascade. The position of the probe was measured using an LVDT transducer that was attached to the traversing assembly. The LVDT had a linear output from –3 to +3 V DC and a input from a power supply of a constant +5 V DC. Figure 2.10 shows a schematic of the data acquisition setup.

The voltage outputs from the pressure transducer box were recorded using Labview data acquisition software. The Labview data acquisition system consisted of a personal computer and multiplexor capable of recording 32 voltage signals and 32 thermocouple signals. The sampling frequency and the number of samples to be recorded per channel were to be input by the experimenter. For this experiment, data was sampled at 100 Hz and 1000 samples were recorded per channel, which resulted in a 10 second sampling period. It should be noted that the Labview Code is a low speed, steady-state measuring system and would not be suited for high-speed measurements such as velocity fluctuations used in measurement of turbulence. The signals

acquired by Labview include: upstream total pressure, differential total pressure, traverse position, and downstream static pressure from the traversing probe. After the PSI system malfunction in the latter stages of this study upstream and downstream sidewall static pressure was also recorded in Labview.

Two other signals were monitored during this testing but were not directly used in the aerodynamic loss calculation. The relative humidity of the air entering the cascade was monitored using a relative humidity sensor. In previous studies relative humidity higher than 10% have been found to increase the total loss level. In addition to humidity sensor, an OMEGA type-K thermocouple was positioned approximately in the same location as the upstream total pressure probe and monitored the total temperature entering the cascade. The output from the thermocouple was recorded and converted to degrees Centigrade by the data acquisition software. Although the total temperature measurement was not essential to the aerodynamic loss calculation it was needed to reduce the turbulence intensity data generated by the turbulence grid, and for the calculation of AVDR.

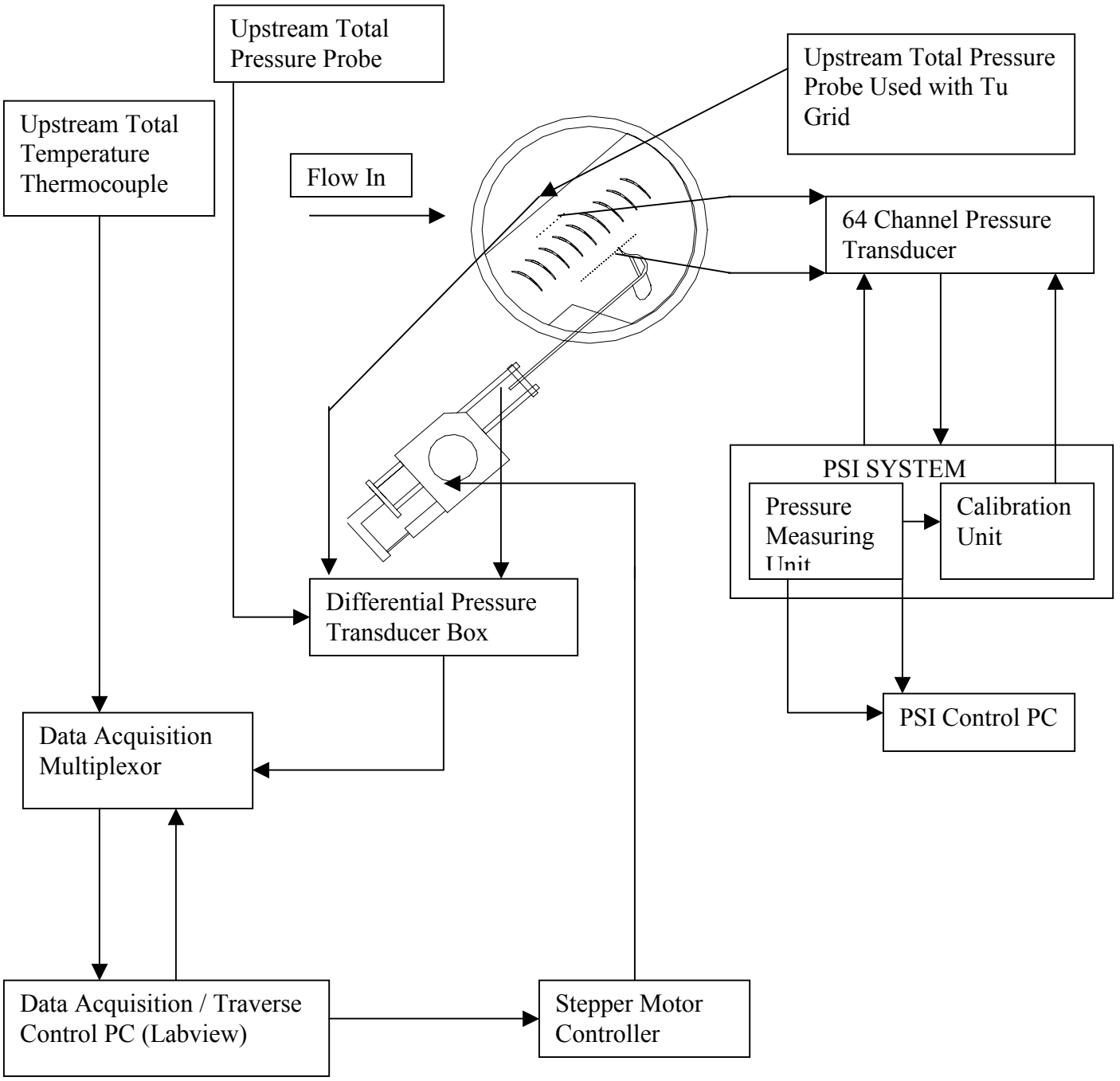

Figure 2. 10 Schematic of Low Speed Data Acquisition

2.4.2 Hot Wire Setup and Measurements

The hot wire used for this work was a standard Dantec probe and was used for previous research at Virginia Tech. The wire is positioned so that the two sets of two prongs are parallel at an angle of 90^{o} to its body (3.2mm stainless steel tubing). The dimension of the wire used was 5㎜ (0.005 mm = 0.0002 inches), and were attached to the prongs using annealed Tungsten, either at the manufacturer or at facilities at Virginia Tech. The hotwire was controlled using a Dantec (55M01) anemometer equipped with a (55M10 CTA) standard bridge accessory. The standard bridge was designed for use with a 5 meter BNC cable and was displayed in a window over the cable compensation controls. A TSI Corp. IFA-100 anemometer was coupled with Dantec anemometer for use of the IFA's signal conditioner. IFA's signal conditioner allowed the signal to be filtered and offset as the flow condition dictates.

The frequency response of the hot wire was adjusted with two controls on the front panel of the Dantec unit. The two controls are labeled "L" and "Q" which is more commonly known as cable compensation. These controls are to be turned clockwise (CW) and counterclockwise (CCW) until the proper test signal is seen on an oscilloscope, as documented in the manufacturer's literature. Over or under adjustment will cause the anemometer to become electronically unstable. This tuning of the frequency response must be performed in a flow similar to the test conditions such that the Reynold's number (Re) of the wire is matched. In general, frequency response increases with the adjustment of the cable compensation, but at an extreme tuning position the system becomes instable. At no flow or low speed conditions a high frequency response was very easily obtainable. However, since the frequency response is sensitive to

Reynold's number, high Re flows cause greater instability and require a lower frequency response, or in other words, a lower cable compensation. For this study the high Re flow condition could not be obtained through bench testing. Therefore, the hotwire's frequency response was tuned inside of the test section of the wind tunnel. Since the run time of the tunnel is approximately twenty seconds at steady-state conditions, this tuning required several iterations.

As mentioned previously, the Labview-based data acquisition system used in the current work, would not be sufficient for high-speed data measurements, such as velocity fluctuations. Data acquisition was performed on a LeCroy-based acquisition system capable of measuring eight channels at high frequency. The sample frequency for this study was set at 50 kHz. After the Dantec anemometer measured the voltage fluctuations, the signal was run through the IFA-100 where the DC component was offset and the signal was filtered. The low bypass filter on the IFA was set at 25 kHz, and the signal was offset 7 VDC for high Mach number tunnel running conditions to provide better resolution of the signal. Once the signal reached the LeCroy and was recorded it was saved and written as an *.ASC file to be input to a Fortran one-point calibration method. This calibration method idea will be discussed in the next section. Figure 2.11 shows a schematic of the measurement system with the hot wire inserted in the test section.

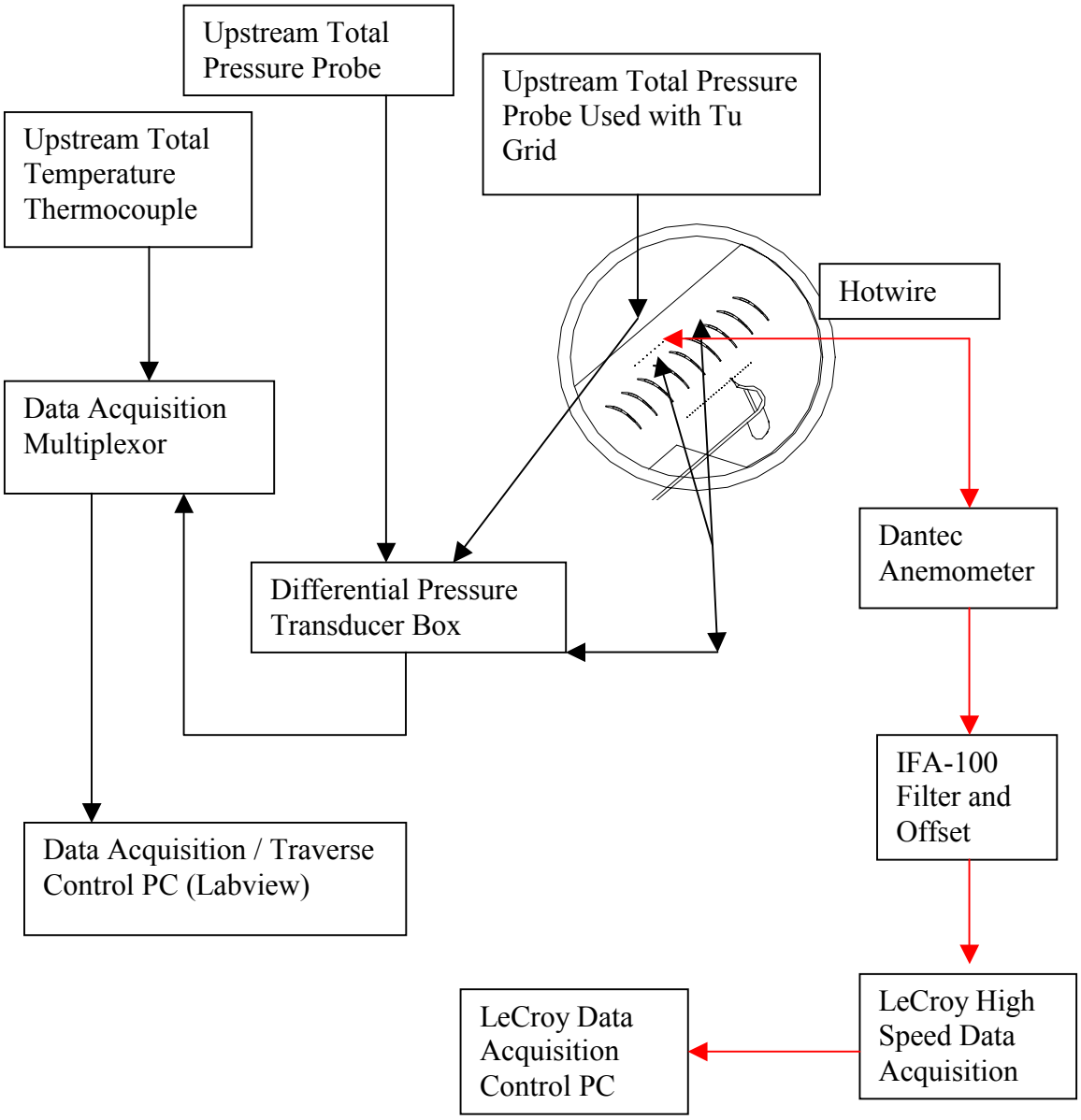

Figure 2. 11 Schematic of High Speed Data Acquisition with Hot Wire

2.4.3 Static Pressure Measurements on the Blade Surface

Static pressure taps were fabricated on both the pressure and suction surfaces of the compressor stators. A photograph of the instrumented stators is shown in Figure 2.12. The static pressure holes were positioned at approximately 4% chord apart, and measure from about 4% chord to approximately 90% chord. Stainless steel tubing 1/16 inch in diameter, was placed into the machined slots using aerospace structural epoxy and then sanded so that the geometry of the stator was unchanged. After assembling the instrumented blades into the Plexiglas side walls, they were checked for leaks using Snoop leak detector. Since each blade is instrumented with 18 static pressure holes, the leakages of one or two taps was not catastrophic to the experiment and therefore, were abandoned. Each static pressure was measured with an individual differential pressure transducer and recorded with the low speed data acquisition system. The range of these measuring transducers was from +/-5psig to +/-15psig.

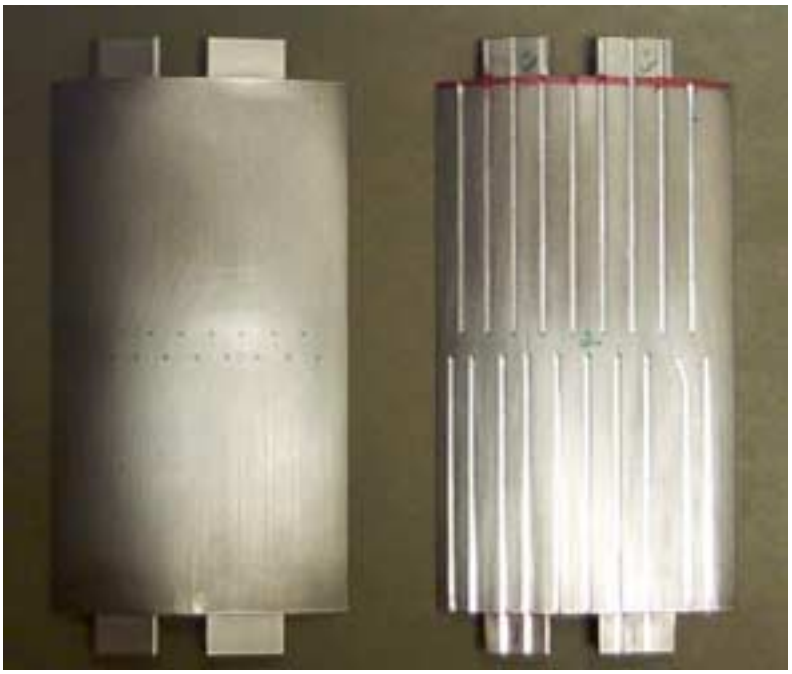

Figure 2. 12 Instrumented Static Pressure Stators

2.5 Oil Flow Visualization

An efficient technique for gaining a physical picture of the flow pattern for qualitative analysis is the use of surface oil flow visualization. Surface oil visualization involves coating the blade surfaces and Plexiglas sidewalls with contrasting fluorescent colored paint. The paint is made up of a mixture of oil and dye, and is mixed at 3:1 oil to dye. After the painted cascade is assembled it is inserted into the test section and the tunnel is run at a know pressure and Mach number. The pattern of oil formed by the mass flow through the test section on the blade surface and sidewall is used to qualitatively analyze the cascade flow field. Even though this pattern can be easily seen under normal light, a fluorescent light is used when taking still photographs to make the pattern even more distinguishable. The oil visualization is very helpful to examine the effects of flow separation, probable shock location, and secondary flow. The qualitative analysis of these flow phenomena makes the measured aerodynamic properties easier to explain and understand. Figure 2.13, provides an example of this technique in a picture of the entire cascade, however, more detailed pictures will be included in the next chapter of this work.

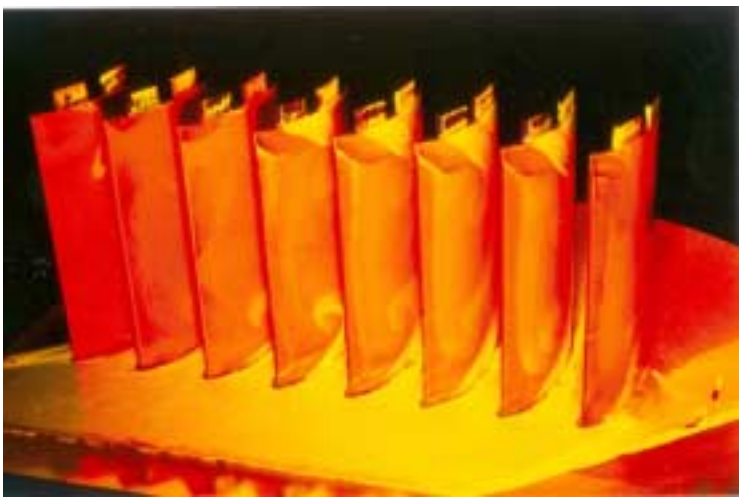

Figure 2. 13 Oil Visualization Entire Cascade

2.6 Data Reduction

Two testing techniques were used to analyze the aerodynamic performance of the cascade tested in this work. One method used was the monitoring of the pressure loss calculation to provide a quantitative measure of cascade performance. The second method used was oil visualization and this method was used to qualitatively explain the quantitative results. Obviously, three-dimensional flow exists in any passage of the cascade, but only two-dimensional effects were examined in both the pressure loss coefficient and the oil visualization.

2.6.1 Pressure Loss Coefficient

There are many variations for expressing the pressure loss coefficient through a cascade. Equation 2.5 is the integral from of the pressure loss coefficient through the cascade used in this work. The loss coefficient was calculated and area-averaged over one passage as defined for a compressor blade passage. Pt1 is used for simplicity for the upstream total pressure, it is Pt_{1cas}, for all turbulent grid testing scenarios.

$$\omega = \left[\frac{\int_{mid-passage-A}^{mid-passage-B} \left(\frac{P_{t1} - P_{t2}}{P_{t1} - P_{s1}} \right) dy}{\int_{mid-passage-A}^{mid-passage-B} dy} \right]$$

Equation 2. 5

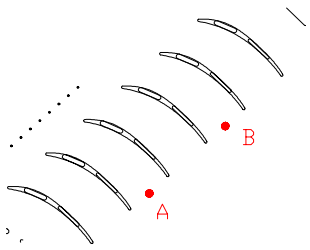

Figure 2. 14 Measured Center Passages

The two center passages were measured in the cascade so that the potential flow effects from the top and bottom wall would be minimal. The loss coefficient is calculated and averaged for each passage individually, and then an arithmetic average is calculated for the combined loss through

both passages. This is done because the flow in both passages is not exactly identical and this slight difference is recorded and averaged. The static pressure measurements taken upstream of the leading edge of the stators to be examined were time averaged over the ten second data acquisition window and in the steady-state portion of the running of the wind tunnel. The static pressure readings have an insignificant fluctuation over this time, therefore, making this average acceptable. The downstream total pressure is measured over the two passages to be examined and therefore is dependent upon pitch-wise location. The total pressure difference between state 1 (upstream) and state 2 (downstream) is calculated at the respective instantaneous time and position of the downstream traverse. The upstream total pressure measurement was made at single location because the upstream flow was found to be uniform during the upstream traverse testing mentioned previously and is also time averaged.

Once the upstream static and total pressure measurements are time-averaged the inlet Mach number is calculated using the following equation:

$$\frac{P_{t1}}{P_{s1}} = (1 + \frac{\gamma - 1}{2} \cdot M_1^{\,2})^{\frac{\gamma}{\gamma - 1}} \qquad \textbf{Equation 2.6}$$

The local exit Mach number is calculated in the same manner using the following substitution of states:

$$\frac{P_{t2}}{P_{s2}} = (1 + \frac{\gamma - 1}{2} \cdot M_2^{\,2})^{\frac{\gamma}{\gamma - 1}} \qquad \textbf{Equation 2. 7}$$

This exit Mach number is dependent on the pitch-wise location of the downstream traverse. This measurement was very convenient due to the three-hole traversing probe that had the capability to measure both total and static pressure at the same point. g=1.4 was used for all calculations.

From the measured upstream total temperature and the calculated inlet Mach number the upstream static temperature can now be calculated from the following equation:

$$\frac{T_{t1}}{T_{s1}} = (1 + \frac{\gamma - 1}{2} \cdot M_1^{\ 2}) \qquad \textbf{Equation 2.8}$$

Now with the upstream static temperature, the density can be calculated from the ideal gas law as:

$$\rho = \frac{P_{s1}}{R \cdot T_{s1}} \qquad \textbf{Equation 2.9}$$

Hence, the inlet velocity can be determined using the speed of sound relation in Equation 2.10.

$$U_1 = \frac{M_1}{\sqrt{\gamma \cdot R \cdot T_{s1}}} \qquad \textbf{Equation 2.10}$$

This velocity is based on free-stream measurements and is no indication of the velocity profile to the inlet of the cascade. The Axial Velocity Density Ratio (AVDR) was calculated for this cascade using the following equation:

$$AVDR = \left[\frac{\int_{mid-passage-A}^{mid-passage-B} (\rho_2 \cdot U_{A2})_{MS}\, dy}{\int_{mid-passage-A}^{mid-passage-B} (\rho_1 \cdot U_{A1})\, dy} \right] \qquad \textbf{Equation 2.11}$$

The AVDR is a measure of the two-dimensionality of the flow through the cascade. It is also an indication of the flow turning through the passage between two blades. The pressure loss coefficient is often found to be inversely proportional to the calculated AVDR for a cascade.

2.6.2 One-Calibration and Turbulence Intensity

The one-point calibration theory was taken and developed from Homberg (1996) and its details will be included in the appendix of this work. The basis of this calibration is the following equation:

$$Nu \cdot \left(\frac{Tm}{Ts} \right)^{-0.17} = 0.48 \cdot \mathrm{Re}^{0.51}$$ **Equation 2.12 (Holmberg, 1996)**

where (Tm/Ts) is a temperature correction factor, and the Reynolds number has to be greater than 44. The restriction on the Re number is because Re = 44 is the point where laminar to turbulent transition for flow over the wire occurs (Holmberg, 1996). Holmberg (1996) goes into eloquent detail of the validity of the assumptions in using Equation 2.12 for one point hotwire calibration. Putting each piece of Equation 2.12 into known measured quantities, and into a form that can be used for calibration yields the following equation:

$$Nu = \frac{h \cdot d}{k_m}, \quad \text{where} \quad h = \frac{(power)}{(area) \cdot (\Delta T)} = \frac{\left(\frac{V^2 \cdot R_w}{(R_w + R_1)^2} \right)}{(\pi \cdot d_w \cdot L_w) \cdot (T_w - T_s)}$$ **Equation 2.13 (Holmberg,1996)**

where, V is the hot wire(HW) voltage and the tunnel static temperature Ts, are the only variables. All manufacturer given wire properties should stay constant in theory, due to the use of a constant temperature anemometer. So if constant wire temperature (Tw), is maintained then constant resistances should also be maintained (Holmberg,1996). Therefore the Nusselt number equation reduces to: since (Tw - Ts) = 2(Tm – Ts)

$$Nu \propto \frac{V^2}{(T_w - T_s) \cdot k_m} \propto \frac{V^2}{(T_m - T_s) \cdot k_m}$$ **Equation 2.14 (Holmberg,1996)**

Now, substituting Equation 2.14 into Equation 2.12, taking the constant wire diameter out of Re, transposing left and right sides for convenience, and inserting a calibration constant yields:

$$\left(\frac{\rho_m \cdot U}{\mu_m}\right)^{0.51} = C \cdot \frac{V^2}{(T_m - T_s)\cdot k_m} \cdot \left(\frac{Tm}{Ts}\right)^{-0.17}$$

Equation 2.15 (Holmberg,1996).

Simplified to:

$$\mathrm{Re}' = C \cdot Nu'$$

Equation 2.16 (Holmberg,1996).

Equation 2.16 was used for the calibration of the HW for all turbulence grid measurements. The general step-by-step procedure for applying these equations is as follows (Holmberg,1996).

Find the average P_t, T_t, and V (HW voltage) over the selected HW sample.

Solve for T_s, using the isentropic relationship with the known inlet Mach number and $\gamma = 1.4$ as the initial value.

Calculate what your new Cpair based on the following variable specific heat equation:

$$Cp_{air} = 1037.8 - 0.22371 \cdot T_s + 2.8556x10^{-4} \cdot T_s^2 + 5.2694x10^{-7} \cdot T_s^3 - 5.3327x10^{-10} \cdot T_s^4 \quad \left(\frac{m^2}{s^2 \cdot K}\right)$$

Equation 2.17 (Holmberg, 1996).

Proceed now to calculate a new γ, P_s, T_s, U, T_m, ρ_m, μ_m, k_m, Re', Nu', and finally the calibration constant C. These values are found using basic compressible flow and heat transfer equations.

This calculated constant C is for the HW used, and will remain constant from run to run, with some small drift over time. This constant can then be used for the conversion of all the HW bridge voltage data acquired in that run to a velocity series. It should be noted that this documented procedure is an abridged version and that a detailed procedure is documented in Holmerg's (1996) dissertation attached in the appendix of this work.

When using the above calibration to solve for the velocity, the values of Re' and Nu' must be solved iteratively with the help of a small FORTRAN code (Holmberg,1996). The code used in this work is Fortran Powerstation and will be included in the appendix. The progression is similar to above calibration equations, but the result is U for each sampled data point instead of a calibration constant (Holmberg, 1996). The following procedure leads to the instantaneous velocities:

Solve for Cp, T_s, T_m, k_m, μ, ρ, as above.

Solve for Mach number, M.

The Ps = f(Pt, γ, M).

Solve for Nu' using the instantaneous HW voltage.

$$(\rho \cdot U) = \mu \cdot (C \cdot Nu')^{\frac{1}{0.51}}$$, where Re' = C*Nu'

Mean density from the low speed data, $P_{s,m}/R*T_s$

Then instantaneous U= $(\rho *U)/\rho_m$ if density fluctuations are assumed negligible.

Iterate the above sequence until U converges to a solution.

Once a solution for instantaneous velocity, U, is obtained for each instantaneous voltage, then a turbulence intensity (Tu) can be obtained using the entire velocity series as demonstrated by the following equation:

$$Tu\% = \frac{u'}{U} \qquad \textbf{Equation 2.18}$$

where U is the mean velocity and u' is the Root Mean Square(RMS) of the fluctuating component of the velocity. The definition of any instantaneous velocity recorded in time is as follows:

$$\tilde{u} = U + u \qquad \textbf{Equation 2.19}$$

where U is the mean velocity and u is the fluctuating component. The RMS of the fluctuating component is defined by the following equation:

$$u' = \left(\frac{1}{N} \cdot \sum_{i=1}^{N} u_i^{\,2} \right)^{\frac{1}{2}} \qquad \textbf{Equation 2.20}$$

where N is to the total number of velocity measurements taken in a given sample.

The turbulence scale was calculated with the following method. First, the autocorrelation (R_v) of the fluctuating component of velocity (normalized such that R_v is equal to 1 at zero lag, t=0) was calculated by the following equation:

$$R_v(\tau) = \left(\frac{\overline{u(t) * u(t+\tau)}}{u'^2} \right) = \frac{1}{N} \cdot \left(\frac{\sum_{i=1}^{N} u_i \cdot u_{i+1}}{u'^2} \right)$$ **Equation 2. 21 (Sauer,1996)**

where $\tau = j \cdot \Delta t$ for j=0,1,2…N. The autocorrelation was used to determine the integral time scale (T) by integrating under the curve to the first zero crossing, demonstrated in the following equation:

$$\mathrm{T} = \int_{t=0}^{\infty} R_v(\tau) d\tau = \sum R_{vi} \cdot \Delta\tau$$ **Equation 2. 22 (Sauer,1996)**

where N_o is the point of the first zero crossing. The streamwise integral length scale (L_x), which is representative of the largest eddies in the turbulent flowfield, was then determined by invoking Taylor's hypothesis of frozen turburlence in the following equation:

$$\Lambda_x = U \cdot \tau$$ **Equation 2. 23 (Sauer,1996)**

The code used for the calculation of the turbulence scale will be included in the appendix of this work.

Chapter 3 EXPERIMENTAL RESULTS AND DISCUSSION

This chapter will review and discuss the results obtained from cascade experiments with and without increased free-stream turbulence at varying cascade angles and inlet Mach numbers. Section 3.1 discusses the turbulence level results obtained from the hotwire measurements, while section 3.2 will display and discuss the aerodynamic performance data recorded for the varying experimental scenarios. At the end of each of the respective sections, work from previous researchers will be compared to the current work to try to explain and validate the recorded data and observable trends found in the results from the current experiment. It should be noted for all data presented in this chapter that incidence angle is denoted as "cascade angle". The angle is referenced to in this manner due to the uncertainty of actual inlet flow angle to the cascade. It is believed from preliminary testing that the inlet flow may be inclined up to 1.5^{o}. It should also be mentioned that the AVDR displayed on the loss coefficient figures is given in a range due to the lack of necessary means to control the AVDR to a constant value.

3.1 Turbulence Level Measurements

Only one passive turbulence grid was used in this experiment, so therefore, the turbulence level generated from this grid was used for all turbulence testing and was compared to the baseline case of no grid generated turbulence. The Reynolds number range of all testing conditions was about $1\text{-}2\text{x}10^{6}$. The baseline turbulence level was measured to be approximately 0.1-0.2%, at all Reynolds' numbers tested. The turbulence level was approximately 1.6% at the lower extreme of the Reynolds' number range, and approximately 1.3% at the higher extreme. The fluctuating velocity plots versus time, are displayed in Figure 3.1 for all of the respective experimental cases.

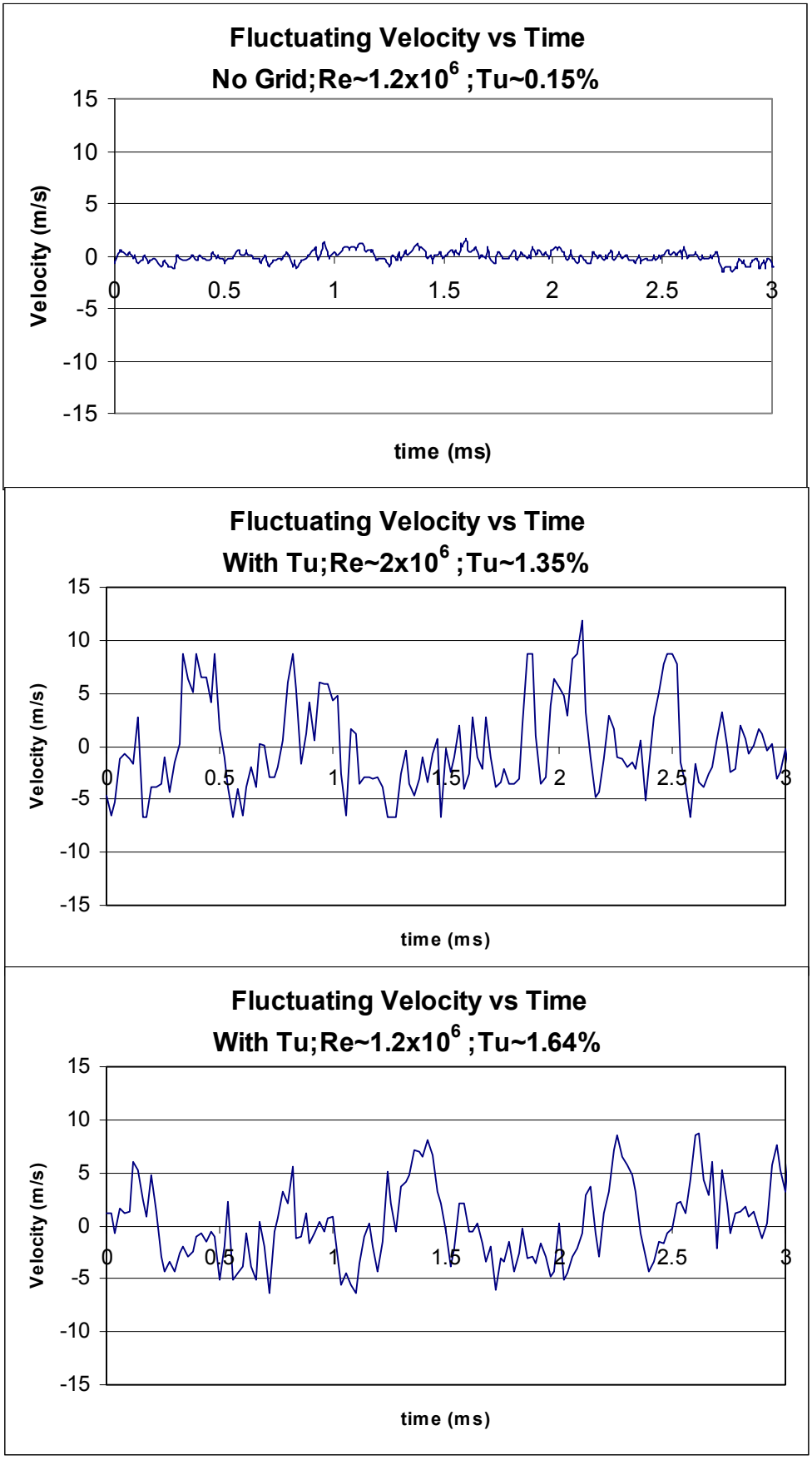

Figure 3. 1 HW Voltage Plots for Respective Tu Intensities

The slight increase in turbulence intensity at lower Reynolds numbers is probably due to the dominance of the inverse relationship of velocity to turbulence intensity in Equation 2.18, whereas, Reynolds number directly proportional to velocity. It should be noted that the details of turbulence and turbulence decay were not the primary focus of the current work, and a detailed analysis of the nature of turbulence was not performed. The effects and influence of the grid generated turbulence on performance was the phenomena of more interest. However, it is worth comparing the measured turbulence level with that of the turbulence level predicted by the 5/7 Power Law, for which the turbulence grid was designed.

	5/7 Power Law (*Equation 2.1*)	Measured TU Value	Calculated Tu Scale, L_x
Turbulence Intensity	5.2%	1.3-1.6%	~1.7 cm

Table 3. 1 Comparison Between Predicted and Measured Tu Intensity

Table 3.1 shows that the 5/7 Power Law (Equation 2.1) severely under-predicted the turbulence decay for the turbulence grid in this study. This under prediction is probably not due to an erroneous Power Law, but is probably because the grid used in this work was located immediately upstream of a convergent nozzle. Although Equation 2.1 is independent of mean velocity, the calculated turbulence intensity (Equation 2.18) is inversely proportional to the mean velocity. Since the flow is accelerated through the contraction, the mean velocity is significantly higher. If it is assumed that the fluctuating component of velocity in Equation 2.18 will remain constant through the contraction, then the absolute turbulent intensity will be forced lower. From a relative perspective, the degree of the actual turbulent fluctuations would be the same as if the duct walls were parallel, and the mean velocity lower. Therefore, the constant in the 5/7 Power Law (Equation 2.1) would have to be altered for that of a contraction in the current work.

Table 3.1 also shows the calculated integral turbulence scale for this work, which stayed very close to constant since the grid was only located in one position with only one diameter of bars. Since the nature of turbulence is beyond the scope of this work, little previous research was examined in order to validate any speculation on the effects of the contraction or the scale. However, Kiock(1972) had documented the inverse relationship between Reynolds number and turbulent intensity. During his experiments on a six-stage axial compressor, Kiock found that when Reynolds numbers where on the order of $2x10^5$, that turbulence intensity was found to be only 3%. When operating his experiment at a Reynolds number of $0.6x10^5$, Kiock found that the turbulence intensity had increased to 5%. Since the current testing covers a smaller range of Reynolds number, the small variance in turbulence intensity is feasible.

3.2 Aerodynamic Data Regarding Performance and the Boundary Layer

3.2.1 Total Pressure Loss Coefficient

The behavior of the total pressure loss coefficient was the parameter of primary focus in the current work. The pressure loss coefficient will be displayed in the following figures versus cascade angle for a given inlet Mach number. A summary will also be given for the pressure loss coefficient versus inlet Mach number to show the trend of performance as a function of a different parameter. The following figures will include the trend for both baseline and generated turbulence running conditions. The pressure loss coefficient is based on area averaged downstream total pressure traverse of the center two passages in the cascade. The loss coefficient was interpolated when necessary to fit the plot format in the following figures.

Figure 3. 2 Loss Coefficient vs. Incidence for Inlet Mach Numbers 0.60, 0.65, 0.70, 0.75

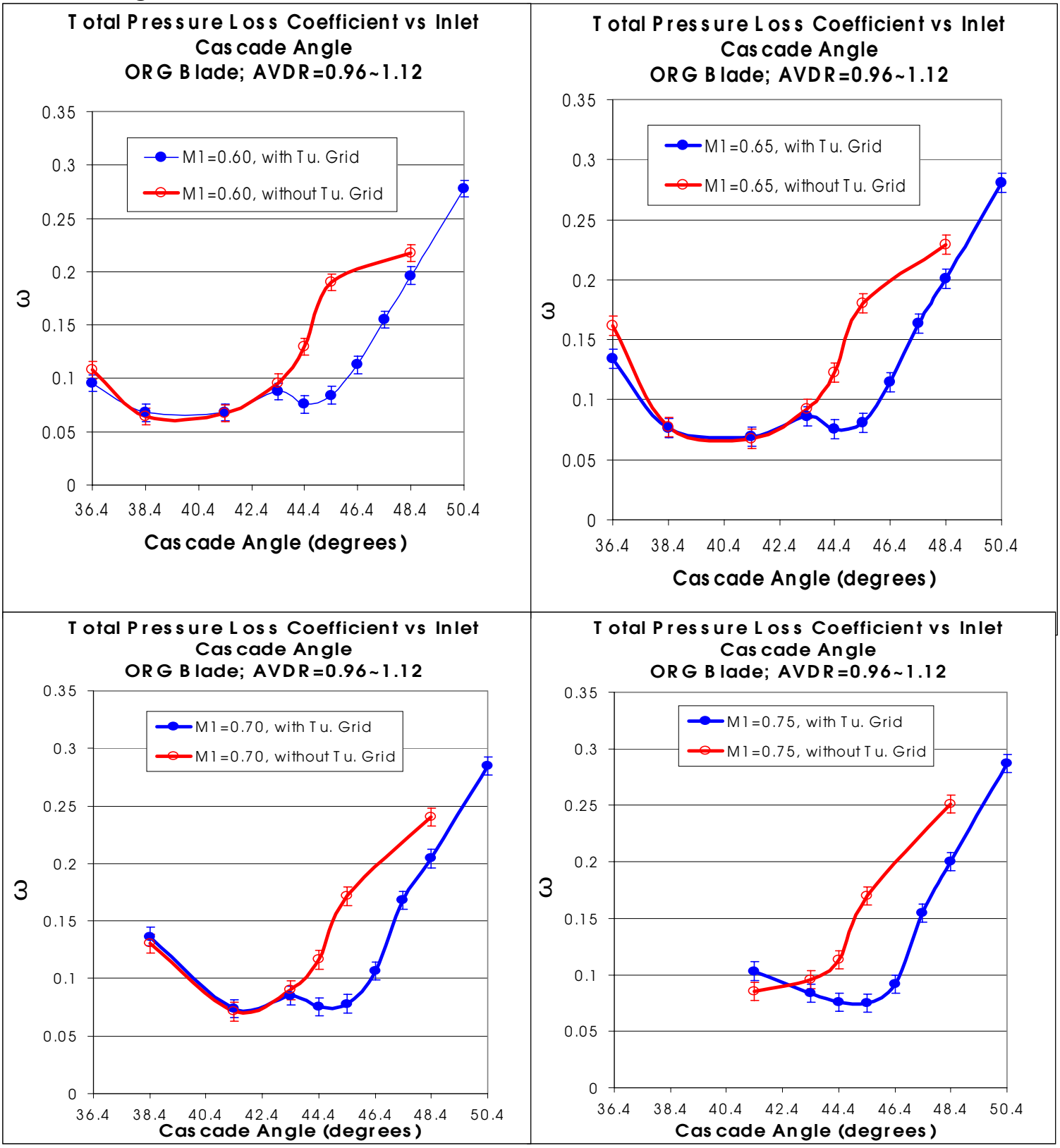

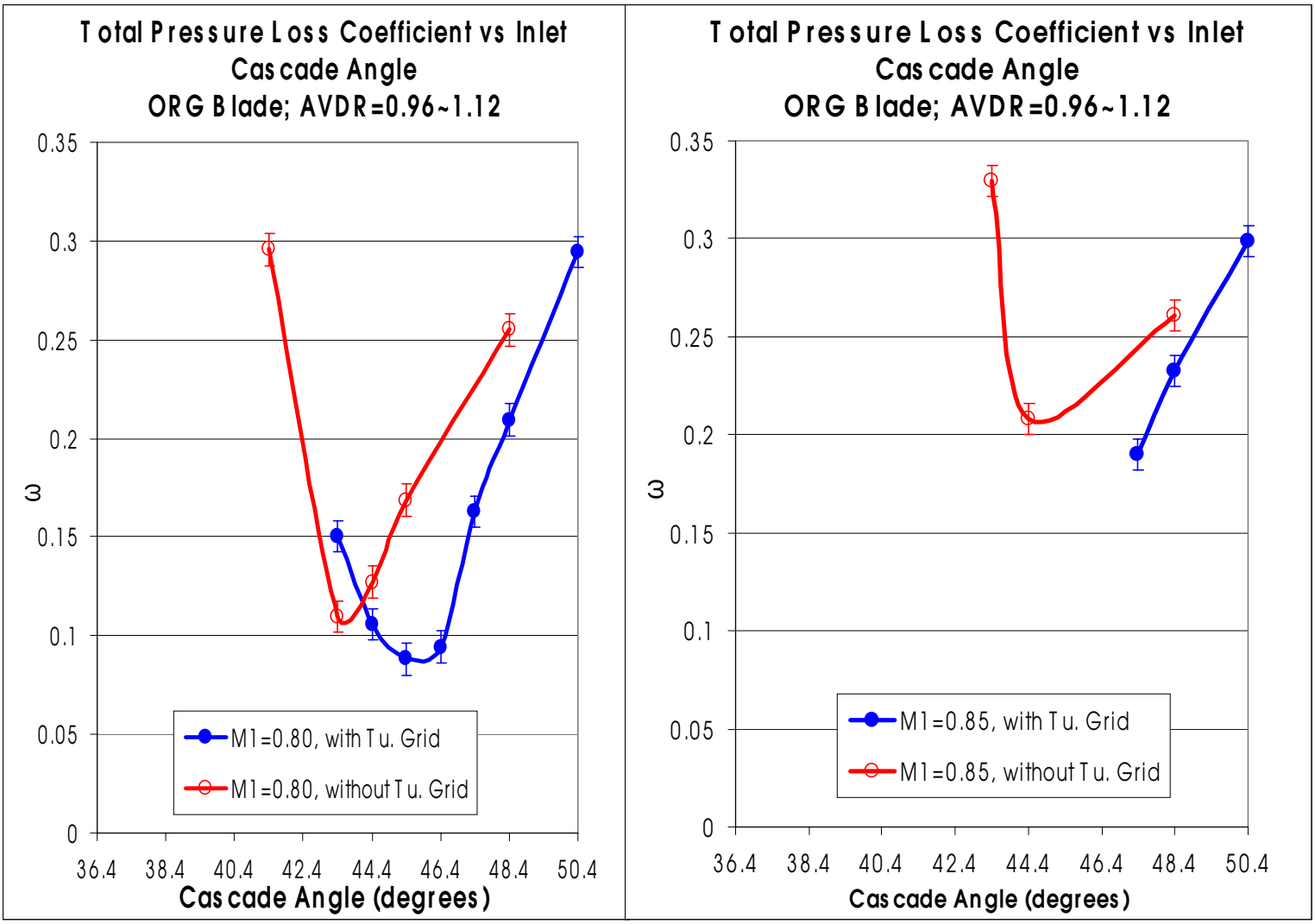

Figure 3. 3 Loss Coefficient vs. Incidence for Inlet Mach Numbers 0.80, 0.85

3.2.1.1 Effects of Turbulence on the Loss Coefficient at Negative Cascade Angles

Figures 3.2 and 3.3 clearly display the effectiveness of increased free-stream turbulence, particularly at positive cascade angles. It should be noted that Figure 3.3, inlet Mach number 0.85, that results at 46.4° and lower could not be obtained because the cascade was choked trying to obtain this inlet condition. It should also be noted that through preliminary loss coefficient testing at the baseline condition, the lowest loss level for the widest range of inlet Mach number was found to be at a cascade angle of 44.4°, so all subsequent testing was referenced and hinged around this cascade angle. In Figure 3.2 at low inlet Mach numbers, it seems that a cascade

angle of 43.4^{o}, is a critical cascade angle where the effect of free-stream turbulence on the loss coefficient starts to become negligible for remaining negative cascade angles. This negligible effect of turbulence at intermediate to low Mach numbers, and negative incidence, may best be explained by the possibility that the flow is not separated from the blade surface at either the baseline condition or with generated turbulence. Therefore, even if the transition point is moved by the free stream turbulence, any reduction in losses due to delayed separation cannot be realized. It should be noted that no oil visualization was done at cascade angles below 44.4^{o} , and limited visualization was done at 44.4^{o} due to time restrictions. Therefore, the above speculation cannot be effectively supported. This condition of nonseparated flow may best be represented in Figure 3.4.

Figure 3. 4 Oil Visualization, I=44.4^{o}, M1~0.65

Figure 3.4 is a picture of the suction side of a stator located in the center passage of the cascade. This stator was tested at a cascade angle of 44.4^{o} and an inlet Mach number of approximately 0.65, with generated free-stream turbulence. It appears from Figure 3.4 that flow at the mid-span of the blade is attached over the full suction surface. Since Figure 3.2 shows some reduction in losses for this cascade angle and inlet Mach number, the baseline testing condition probably has some small turbulent separation near the trailing edge of the stator. Whereas, with generated turbulence, turbulent separation appears to have been totally eliminated at mid-span. It should be noted that the suction surface of the blade was painted from 0-50% chord(pink), and the pressure side painted from 50-100% chord(yellow) in order to try to ascertain flow direction. From Figure 3.4, it may be reasonable to assume that at negative cascade angles the trend of completely attached flow is developing. This leads to the negligible differences in the loss coefficient with and without generated turbulence at negative cascade angles.

At an inlet Mach number of 0.75 in Figure 3.2 and an inlet Mach number of 0.80 in Figure 3.3, the effect of free stream turbulence at negative cascade angles, is seen to be that of an adverse one. Since no visualization or blade surface static pressure measurements were conducted at these cascade angles, the author can only speculate based on Figure 3.3 that the increased turbulence may have caused a higher degree of separation. This may be because these cascade angles and inlet Mach numbers are approaching the stalling point of the cascade.

3.2.1.1 *Effects of Turbulence on the Loss Coefficient at Positive Cascade Angles*

From Figures 3.2 and 3.3, the cascade angle range of 44.4-48.4°, a substantial loss-reduction is realized for all inlet Mach numbers tested. It may now be helpful to the reader's perspective to re-plot the loss coefficient versus inlet Mach number for the two extremes of the incident angle range previously mentioned.

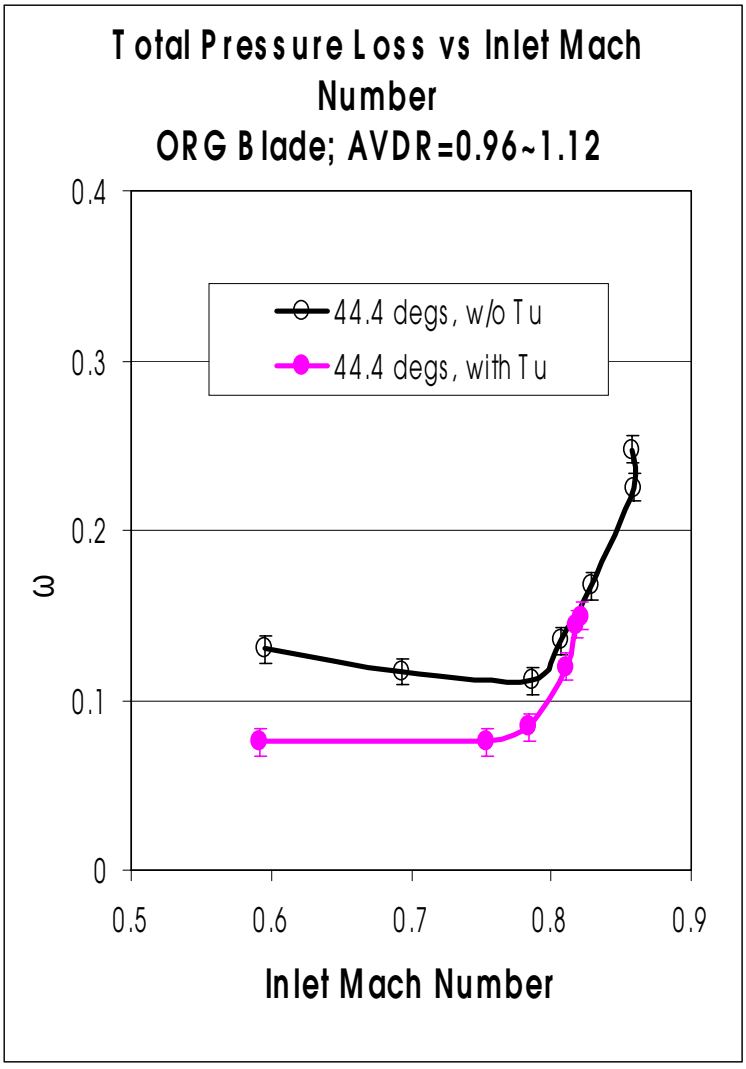

Figure 3. 5 Loss vs M1; *I=44.4°*

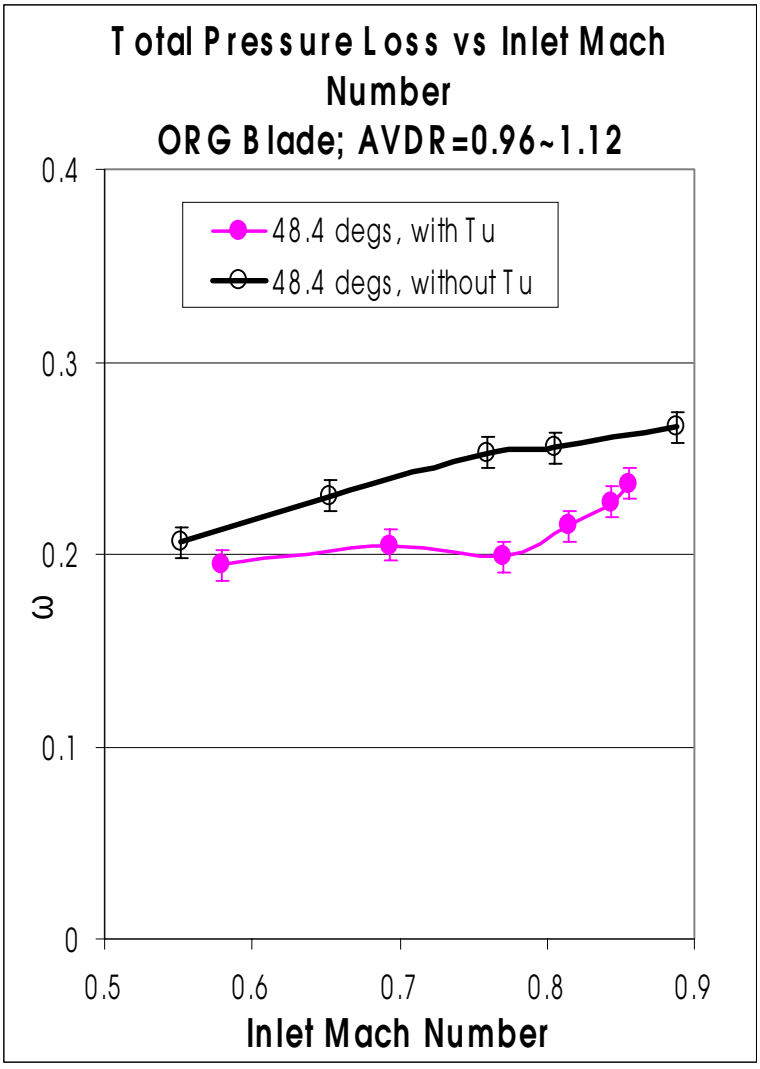

Figure 3. 6 Loss vs M1; *I=48.4°*

Figures 3.5 and 3.6, may make it more visually apparent to the effects of increasing free-stream turbulence on cascade performance. Table 3.2 is a summary of the percentage loss reduction for Figures 3.2, 3.3, 3.5, and 3.6 at positive cascade angles.

M1 ↓	44.4°	45.4°	46.4°	47.4°	48.4°	Cascade Angle ←
0.6	42%	56%	44%	26%	13%	Loss Reduction ← ↓
0.65	37%	55%	42%	24%	11%	
0.7	35%	54%	46%	23%	17%	
0.75	34%	56%	54%	31%	20%	
0.8	17%	50%	52%	28%	18%	
0.85	NA	NA	NA	22%	11%	

Table 3. 2 Summary of Loss Reduction

Table 3.2 shows a summary of the loss reduction due to effects of increased free-stream turbulence at the experimental "hinge" point through four degrees of positive cascade incidence. In general, the loss reduction shown in Table 3.2 is probably due to the delay in turbulent separation on the blade suction surface. This delay may best be explained by the suppression of the laminar separation bubble with increasing free-stream turbulence. With this suppression, the turbulent portion of the boundary layer will cover more of the blade's surface, making the boundary layer more tolerant to the adverse pressure gradient over the airfoil. The first noticeable trend in Table 3.2, with the exception 45.4°, is that with increasing cascade incidence the effectiveness of generated turbulence on losses is dramatically reduced at a given inlet Mach number. In general, this trend may best be explained by the probability that the location of transition and turbulent separation generally propagate toward the leading edge of the blade with

increasing incidence. With the addition of generated free-stream turbulence, the extent of the forward propagated transition may be further suppressed, allowing the separation of the turbulent boundary layer to be delayed. Even with increasing inlet Mach number, the cascade angle of 45.4^{o}, appears to be an optimum cascade angle where turbulence is most effective (Table 3.2). The trend developed with increasing inlet Mach number is one that points to an optimum Mach number of 0.75. At this Mach number, the effect of turbulence on losses seems to be most effective for cascade angles higher than 44.4^{o}. At 44.4^{o} and inlet Mach numbers above 0.75, the loss reduction is found to decrease. This may be because the cascade is approaching or even reaches the point of complete separation on the suction surface of the stators in the cascade. This condition is different for every cascade angle and occurs at different inlet Mach numbers for each of these cascade angles, respectively. When the cascade reaches this condition, the effect of turbulence seems to be a secondary effect to that of a shock wave that could exist in the blade passage. Therefore, the strength of this shock and its interaction with the boundary layer is believed to determine the effectiveness of the generated free stream turbulence on losses at this condition. This topic will be discussed further in the section 3.2.2, where the results from the imbedded static pressure taps in the blade surfaces are presented.

It is now necessary to compare the loss results and trends of the current work with that of previous research. It will be helpful to first compare the loss level of the current work at baseline conditions (No Grid) with the research of Carter (2001), which was performed in the same laboratory and test section of the current work. Carter's research at his baseline condition was performed on stators that had a 4-inch chord, 6-inch span, 2.22 solidity ratio, and a total turning angle of 69^{o} (47^{o}-current work). The design inlet Mach number in Carter's testing was

approximately 0.8 and a blade chord Reynolds number of approximately $2x10^6$. Carter's results will be compared to Figure 3.3 at an inlet Mach of 0.80. Carter's design cascade angle will be compared to the lowest loss level cascade angle (44.4^o), of the current work.

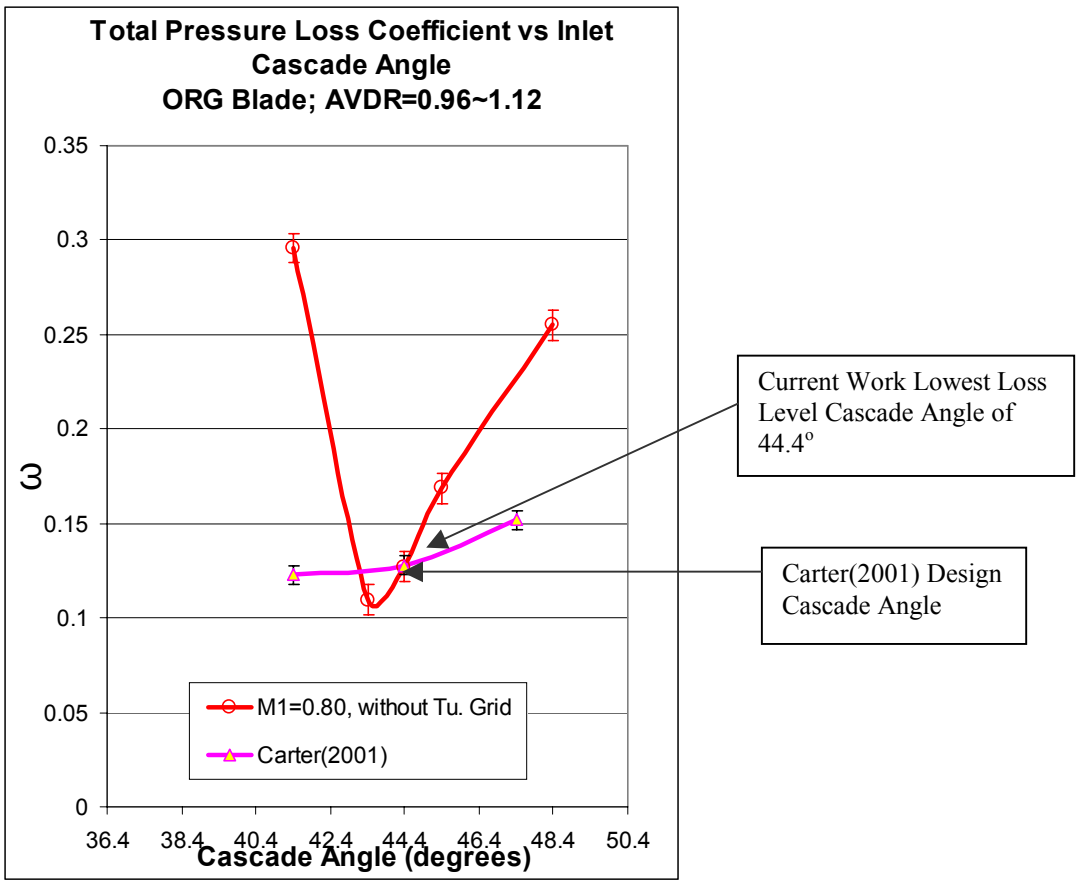

Figure 3. 7 Loss Level Comparison (Carter, 2001)

Figure 3.7 shows a loss level comparison of both the high turning stators of the current work, with that of the even higher turning stators of Carter (2001). The inlet Mach number is 0.80 for both cases displayed in Figure 3.7. It should be reiterated that the lowest loss level for the widest range of inlet Mach number was at a cascade angle of 44.4^o, in the current work, and therefore was used as an "experimental hinge angle" for all-further testing. The loss level at the design cascade angle of Carter's work compares very favorably for that of the current work, while the

off-design angles are quite different. From Figure 3.7, the current work has documented losses below that of Carter's work at a cascade angle of 43.4°. However at angles outside of this 2° range, Carter's stators are far more superior to the stators in the current work. The stators of the current work are depicted in Figure 3.7 to be more sensitive to changes of the cascade angle, in which the extent of the laminar separation bubble on the blade surface plays a major role.

In order to provide insight to the effect of increasing free-stream turbulence on the loss coefficient, the work of Evans (1985) was examined. Evans conducted experiments on a compressor cascade stator that had a chord length of 1 foot, and total turning of 43.65°. At all testing conditions Evans documents that the Reynolds number based on chord was $5x10^5$.

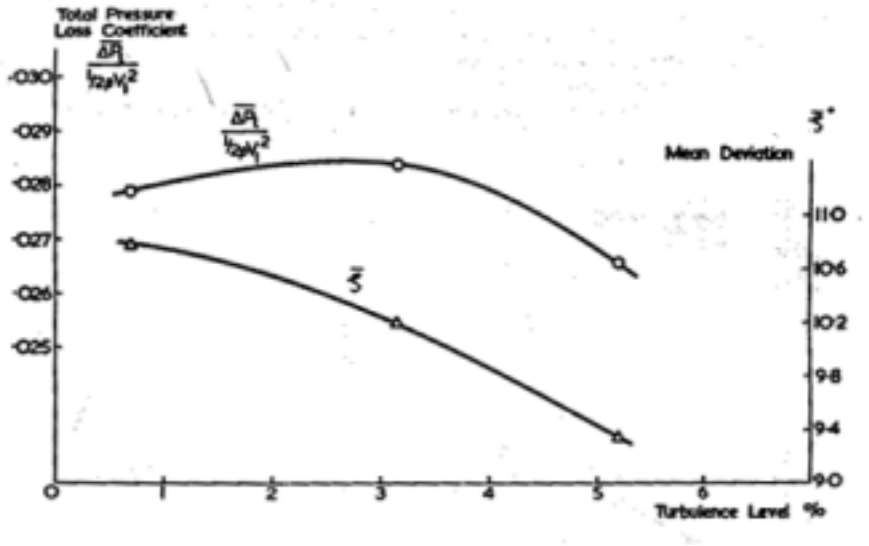

Figure 3. 8 Effect of Tu on Losses and Deviation Angle (Evans,1985)

Figure 3.8 is a summary of the loss and deviation angle reduction that Evans observed with increasing turbulence intensities. Note that he documents a slight increase the loss coefficient at turbulent intensities up to 3%. He credits this behavior to the fact that at lower turbulent intensities the boundary layer displays a thickening behavior. These phenomena will be

discussed further in the next section where the isentropic Mach number distribution will be presented and discussed. At intensities of 3% and higher he notes a decrease in losses. In comparison with the results of the current work, loss reduction was seen at turbulent intensities as little as 1.6%. It is possible that a unique loss reduction curve, as seen in Figure 3.8, exists for different stators, which also may have a different "hypothetical" turbulent intensity where the loss coefficient starts to be reduced. Therefore, only the evidence of the tendency of increased turbulent free-streams as a mechanism to reduce the loss coefficient is relative to this work. It is unknown how a Reynolds number as high as the current work would affect the loss trend in Figure 3.8. Evans further supports his reduction in losses with a measurement of the deviation angle near the trailing edge of the stator. He documents that at all turbulent intensities tested that the deviation angle decreases. In the current work the deviation angle was not measured, but from Figure 3.8, it is reasonable to assume that the deviation angle also decreased with the increasing turbulent free-stream.

The work of Citavy (1977) was also examined in order to gain additional information on the effects of increased free stream turbulence on the loss coefficient of a compressor cascade. Citavy conducted experiments on prescribed velocity distribution (PVD) airfoils at a Reynolds number range of $0.6\text{-}2\text{x}10^5$, and a range of turbulence intensities of 0.35%-4.4%. The PVD had a chord of 140 mm. Again, due to the low Reynolds number range the results are limited in a quantitative sense, but the trend of the results are reasonable for qualitative comparison.

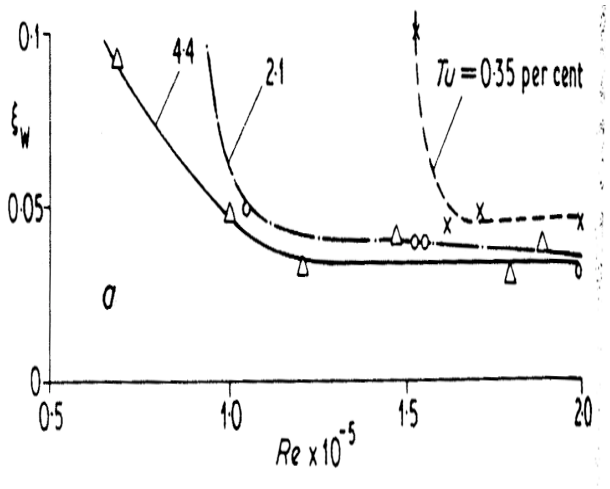

Figure 3. 9 Loss vs. Re(Citavy,1977)

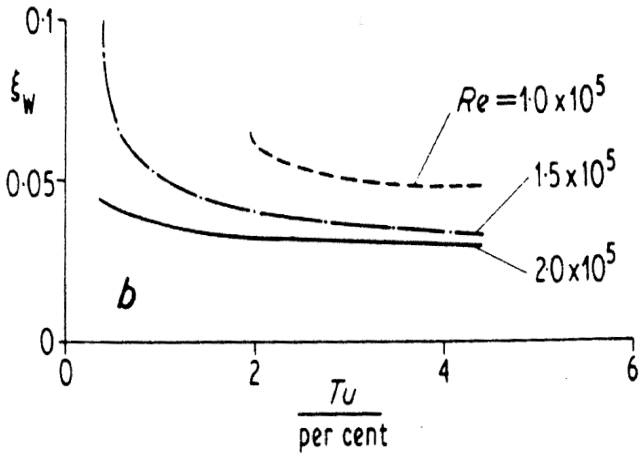

Figure 3. 10 Loss vs. Re(Citavy,1977)

In Figure 3.9 and 3.10, Citavy (1977) displays how the loss coefficient tends to behave as function of Reynolds number and increasing free-stream turbulence, respectively. It is very encouraging that Citavy finds that the largest change loss reduction is found to be the result of only 2% turbulent intensity, as depicted from Tu=0.35 to Tu=2.1 in Figure 3.9. This proves the feasibility of the idea of the effectiveness of increasing free-stream turbulence as loss reducing agent even at turbulent intensities of 1.6%, as in the current work. Moreover, Citavy finds that the largest loss reduction (~50%) at a constant Reynolds number of $1.5x10^5$, is at the intermediate point in his testing. (See Figure 3.10) This trend agrees very well with the current work. In Table 3.2, it is documented that the largest loss reduction is seen at an intermediate inlet Mach number of 0.75, where losses were reduced as much as 56%. It is also significant that Citavy finds that at the higher Reynolds number of $2x10^5$, that the losses become reduced only marginally (~7%) with increasing turbulence levels (See Figure 3.10). This also compares favorably to Table 3.2, where at an inlet Mach number of 0.85 the loss coefficient was reduced less significantly (~11%). It should be reiterated at this point that obviously the stators in Citavy's research were designed for low speeds; however, it is realistic to assume that the trends

that Citavy found might be comparable to a blade design for higher speeds. The most interesting information displayed by both Figure 3.9 and 3.10, is that Citavy observes an asymptotic effect of turbulence on the loss coefficient. Figure 3.10 may be most clear, in that at free-stream turbulence levels between 2%-4% the loss reduction starts to become negligible, even with further increases in turbulent intensity. This suggests that increasing the turbulence intensity in the current research above 1.6%, may not provide an increase in the performance of the stators. The behavior of the boundary layer and its transition is the mechanism for this loss reduction and will be discussed in the next section of this work.

3.2.2 Isentropic Mach-Number Distribution on the Blade Surface

The total pressure loss coefficient provides a quantitative measure for performance through the cascade, but does not reveal any of the flow phenomena that may take place on the actual blade surface. The static pressure taps instrumented in the respective suction and pressure surfaces of the stators may provide some important information to the boundary layer behavior on each blade. In the following figures, the isentropic Mach number distribution will be displayed for cascade angles of 44.4° and 48.4°, respectively.

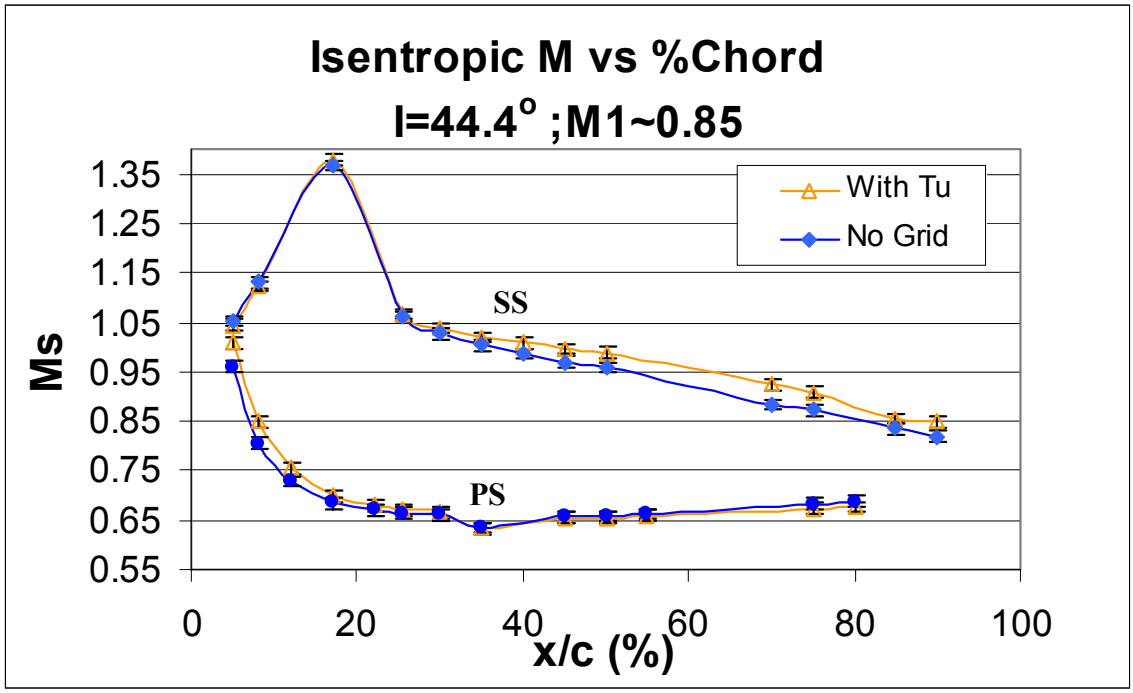

Figure 3. 11 Isentropic Mach Number Distribution I=44.4°

Figure 3.11 shows that at an inlet Mach number of 0.85, the effect of turbulence is that of an adverse one. Although Figure 3.5 shows that losses were obtained only to an inlet Mach number of 0.83, the trend has still developed that the loss profiles have merged and that the loss reduction is nil. Figure 3.11 suggests that at even a slight increase in inlet Mach number to 0.85,

the effects of turbulence increase the degree of separation. The following flow visualization may provide a better picture of the boundary layer activity on the blade surface.

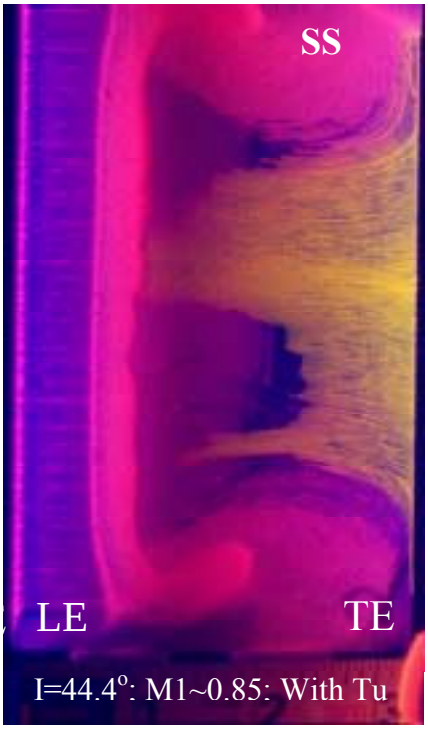

Figure 3. 12 Oil Visualization Choked Condition

Figure 3.12 is a photograph of oil visualization at a cascade angle of 44.4° with generated turbulence. It is clear that reverse flow exists from the pressure side (yellow paint), and that the suction side flow does not reattach. From Figure 3.11, the suction side Mach number at approximately 20% chord is supersonic (Ms~1.35). This suggests that a shock wave probably exists near this point and leads to such a pronounced separation. Free-Stream turbulence seems to have a secondary effect compared with the effect of the shock wave on boundary layer behavior. No oil visualization was performed at this cascade angle for the baseline case, but from Figure 3.5, the high measured losses at baseline probably indicate that the flow is also separated for this same inlet condition.

Since Figure 3.11 suggests that the degree of separation is more dominant with the generation of free-stream turbulence, previous research was sought to explain this phenomena. This phenomena is best documented by Evans (1985), and displayed in Figure 3.13.

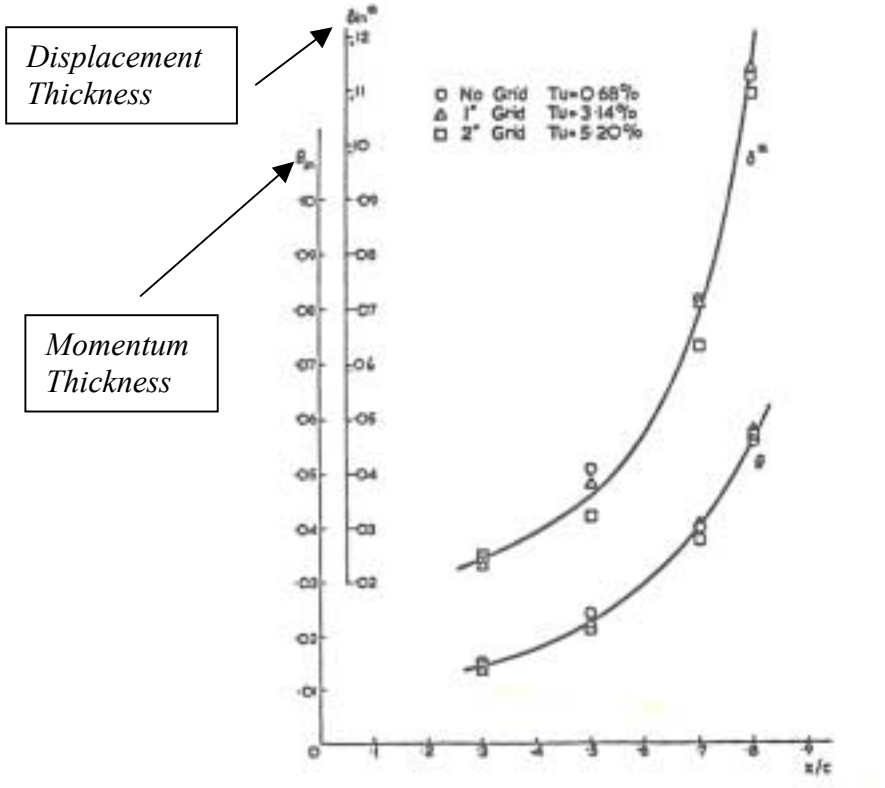

Figure 3. 13 Momentum and Displacement Thickness (Evans,1985)

In Figure 3.13, Evans (1985) documents the momentum and displacement thickness versus % chord for his stator experiments. Evans (1985) performed boundary layer measurements at various chordwise locations on a compressor stator at various intensities of turbulence. Most relevant to the current work, Evans (1985) finds that at chordwise locations close to the separation point, 80% chord in Figure 3.8, that the momentum and displacement thickness increase with turbulence intensities around 3%. At a higher turbulent intensity of 5.2%, the momentum and displacement thickness are again found to decrease. In the current work, with

turbulent intensities of approximately 1.6% and at an inlet Mach number of 0.85, it is probable that this increase in momentum and displacement thickness leads to a higher degree of separation on the stator's suction surface. It should be reiterated that Evans (1985) only recorded this behavior at chordwise locations near separation. At other chordwise locations away from separation, every turbulence intensity tested showed a fuller velocity profile with a decreased momentum and displacement thickness.

The results from the static pressure measurements will now be displayed for the cascade angle of 48.4°. The data will again be displayed as isentropic Mach number versus percentage chord.

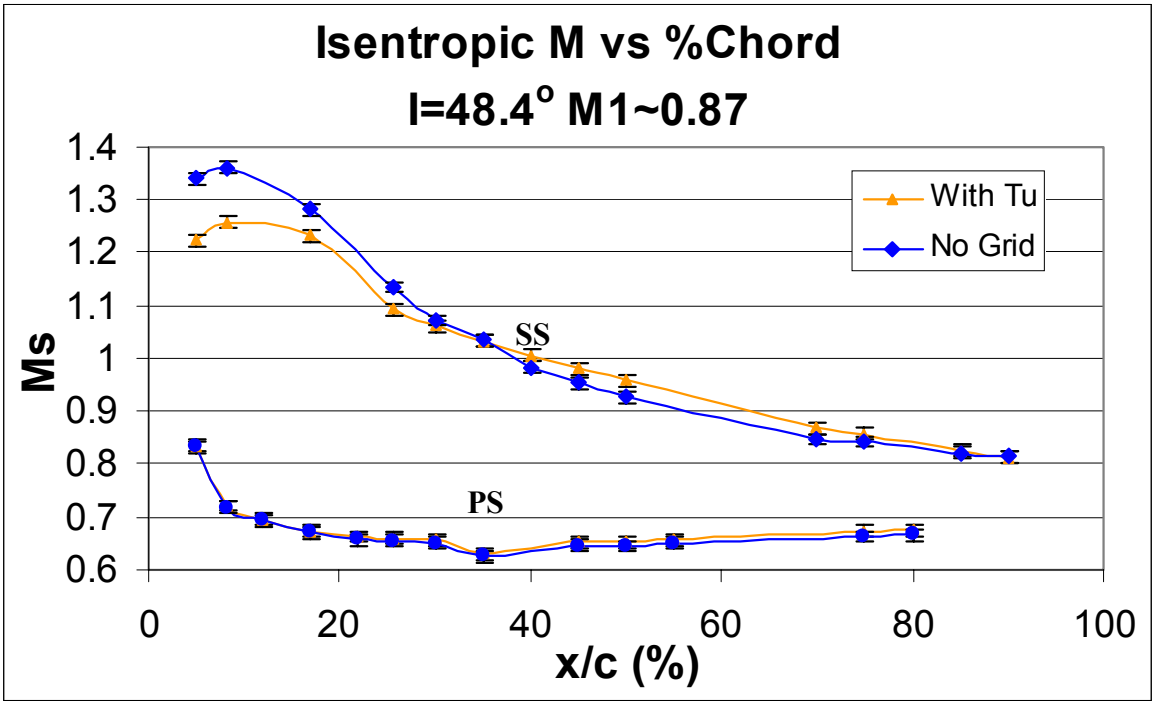

Figure 3. 14 Isentropic Mach Number Distribution I=48.4°

Figure 3.14 shows the isentropic Mach number distribution versus percentage chord for a cascade angle of 48.4°. Figure 3.14 suggests that transition probably exists within a laminar separation bubble and that the effects of the turbulent free-stream have suppressed this bubble. Figures 3.15 and 3.16 may enable more of a mental picture to the boundary layer behavior with and without increased free-stream turbulence.

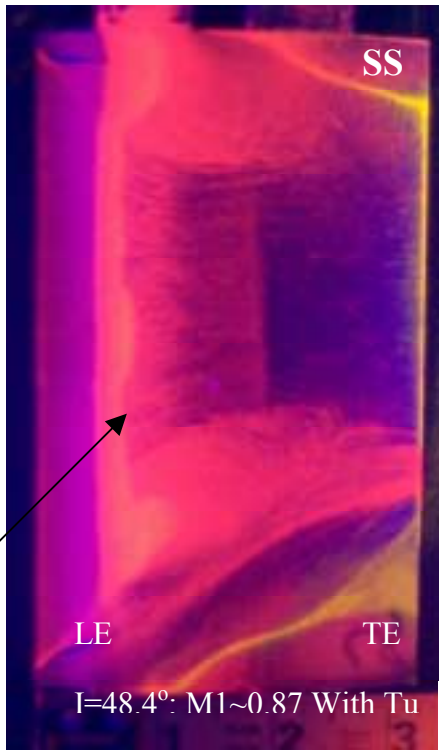

Figure 3. 15 Oil Visualization 48.4° No Tu

Figure 3. 16 Oil Visualization 48.4° WithTu

Figure 3.15 is a photograph of oil visualization at a cascade angle of 48.4°, without increased free-stream turbulence. Figure 3.15 was painted entirely red so even if reverse flow from the pressure side exists it would go unnoticed. One shortfall of oil visualization is that unless contrasting colors are used on the respective surfaces flow direction is impossible to decipher. However, Figure 3.15 does give an idea to the extent of the separation bubble on the suction surface. Figure 3.16, which is a photograph of oil visualization at a cascade angle of 48.4° with

generated turbulence, shows that the laminar separation bubble is indeed shortened with the effects of turbulence. It is obvious from Figure 3.11 that the flow does indeed reattach to the suction surface because of the small portion of reverse flow (yellow paint) from the pressure surface. Figure 3.15 is probably also turbulently reattached to the suction surface as well. In both cases the exact location of reattachment is unknown, but since the generated turbulence forces a shortened separation bubble, it also forces the flow to reattach earlier on the suction surface of the stator. Figure 3.14 further supports this speculation; at 25% chord for the generated turbulent case, the slope of the line changes to one that is more gradual with flow diffusion. Whereas, at baseline conditions, it is not until 30%-40% chord, the slope finally changes to this same trend of gradual diffusion. In each respective case this is probably where the flow reattaches. This probable early reattachment with generated free-stream turbulence, could explain the lower loss coefficient measured for this case and displayed in Figure 3.6. In future research this speculation should be confirmed either with more creative oil visualization techniques or with liquid-crystal visualization. Finally, if a shock does exist near the velocity maximum in Figure 3.14, its strength may not be high enough to cause the boundary layer to separate without reattachment. Furthermore, the effects of turbulence are still observable in Figure 3.14 even if a shock system is present.

It is necessary to first look at previous research pertaining to boundary layer behavior at some range of incidence at constant Mach number. Next, it will then be helpful to examine how the variation of inlet Mach number affects boundary layer behavior. Steinert (1996) examines boundary layer behavior on a CDA cascade with both visualization techniques and blade surface static pressure measurements. Steinert (1996) displays data in a manner that describes both the

effects of changing flow incidence and the effects of varying the inlet Mach number on boundary layer behavior. It should be noted that all of Steinerts' experiments were tested at a constant turbulence intensity of 2%, so that the effects of increasing turbulence were not recorded. However, the documented boundary layer behavior makes Steinert's experiments relative for explaining and validating qualitatively, the probability of results of the current experiment.

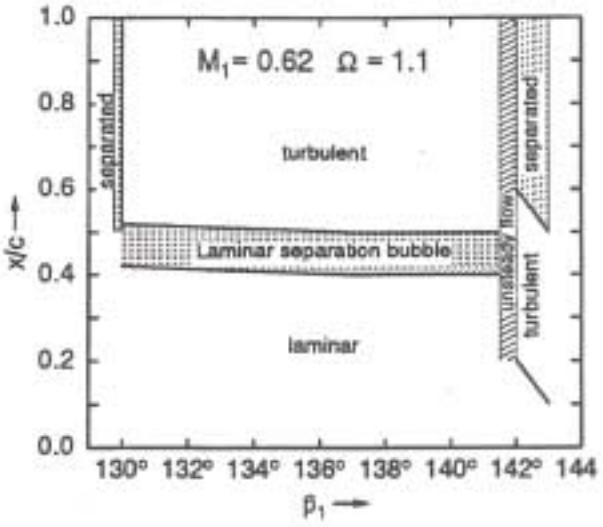

Figure 3. 17 Transition vs b1 (Steinert,1996)

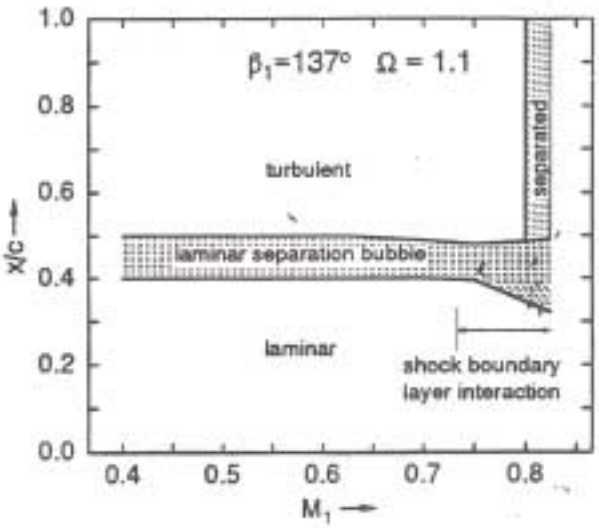

Figure 3. 18 Transition vs M1 (Steinert,1996)

Figure 3.17 shows the boundary layer transition trend that Steinert (1996) saw on the suction surface of his compressor blade at various degrees of incidence. His design incidence was 137^o with respect to the tangential direction. The stators in his experiment were designed for 26.4^o total turning and an inlet Mach number of 0.62. Although stators in the current work are fabricated for 47.2^o turning, it is reasonable to assume that the same pattern of boundary layer behavior may exist at M1=0.65 in Figure 3.2. From Figure 3.2, at a cascade angle of 36.4^o, the cascade is near the same choking point that Steinert reports in Figure 3.17, for an incident angle of 130^o. However, due to the high turning of the stators in the current work it is possible that there is turbulent separation at cascade angle range of 45.4^o-48.4^o. In Figure 3.16 it is evident

that some reverse flow from the pressure side signifies a small portion of turbulent separation. Although no oil visualization was conducted at a cascade angle of 50.4^{o} with turbulence, it is reasonable to assume from Figures 3.2-3.4 that the high loss level at this angle agrees very well with Steinert's unsteady and completely separated boundary layer behavior depicted in figure 3.17, at a positive incident angle of 142^{o}.

In Figure 3.18 Steinert (1996) displays boundary layer transition behavior with varying inlet Mach number at his design incidence angle of 137^{o}. From Figure 3.18, Steinert displays a laminar separation bubble with turbulent reattachment up through an inlet Mach number of about 0.79. At inlet Mach numbers above 0.80, Steinert concludes that the laminar separation bubble is followed by complete separation and that the cascade is in a "choked" condition. Steinert (1996) speculates that this separation is probably caused by a Lambda shock system. Figure 3.18 agrees very well with the results of the current work at a cascade angle of 44.4^{o} , and an inlet Mach number of 0.85, as depicted in Figure 3.12 with complete separation after transition. However, the behavior depicted in Figure 3.18 is not the same for every incidence angle. In the current work, at the more positive cascade angle of 48.4^{o}, as in Figure 3.16, and an inlet Mach number of 0.87, the flow is seen to reattach as a turbulent layer and then turbulently separate very near to the trailing edge of the stator. Since there is probably still a shock present within the passage as suggested by Figure 3.14, it is reasonable to assume that the strength of the shock at this testing condition is not of high enough strength to completely separate the boundary layer after transition, as seen in the case of Figure 3.12 at a cascade angle of 44.4^{o}. Essentially, it is reasonable to assume that the strength of the shock determines the effectiveness of increased

free-stream turbulence on lowering the loss coefficient calculated for the cascade. Steinert's (1996) isentropic Mach number distribution further supports the data of the current work.

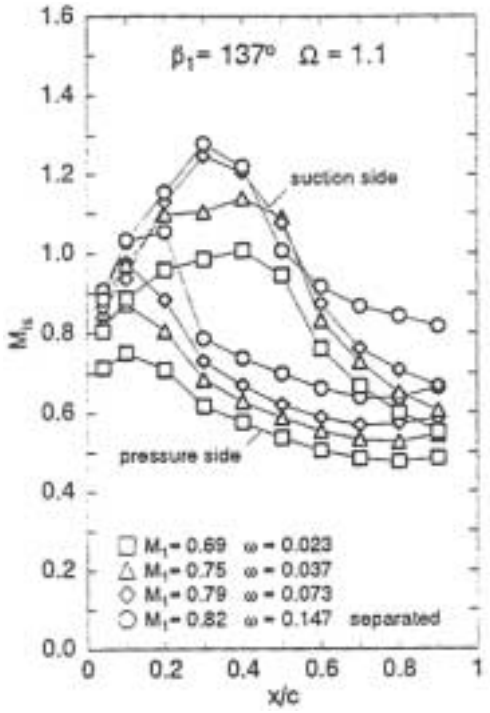

Figure 3. 19 Mach Number Distribution (Steinert,1996)

Figure 3.19 shows a summary of the isentropic Mach number distributions for varying inlet Mach numbers at Steinert's design incidence angle. From Figure 3.19, the maximum Mach number on the suction side of the stator at an inlet Mach number of 0.82 compares favorably with that of the current work for a cascade angle of 44.4^{o} and an inlet Mach number of 0.85, as displayed in Figure 3.11. Steinert records complete separation at 48%-50% chord for this case while in the current work the boundary layer is completely separated at approximately 28% chord. This is probably due to the slight upstream propagation of the separation bubble with increasing inlet Mach number. It is important to point out that from Figure 3.19 at inlet Mach number of 0.79, Steinert displays that the suction side Mach number is supersonic, but it is not

indicated that the boundary layer is completely separated. This supports Figure 3.15 and 3.16 in the current work, the suction side Mach number maximum is supersonic, but the boundary layer is found to reattach turbulently after the laminar separation bubble.

In order to try and explain the effects of varying free-stream turbulence on boundary layer behavior, mainly transition, the work of Schreiber (2000) was examined. Schreiber conducted tests on CDA Airfoils at varying turbulence intensities. The turning of the CDA airfoils was 16^{o} and blade chord was 150mm. The experiment was conducted mostly at a Mach number independent Reynolds number range of $0.7\text{-}2.8\text{x}10^{6}$, and an inlet Mach number of 0.6. Before carrying out experimental boundary layer measurements with the above parameters, Schreiber used the flow-solver MISES to generate a theoretical prediction of transition location and mode at various Reynold's numbers and turbulent intensities.

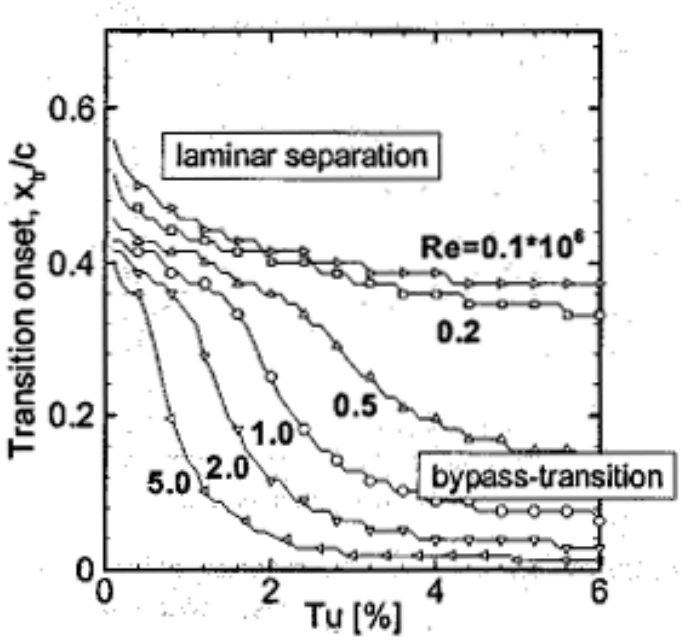

Figure 3. 20 MISES Prediction(Schreiber,2000)

It should be noted that Figure 3.20 is calculated based on the stators in the work of Steinert, and that only the trend of both Figure 3.20 and his results can be compared to that of the current work. Figure 3.20 shows the dependence of transition on both Reynolds number and free stream turbulence. From Figure 3.20, an increase in Reynolds number alone at 0% turbulence can move transition to at least 40% chord, while increasing the turbulence intensity to values of even 1.3% will force transition to approximately 25% chord at a Reynolds number of $2x10^6$. In the current work at a cascade angle of 48.4^o and Reynolds number based on chord of approximately $2x10^6$ based on blade chord, transition was observed at approximately 28% with increasing turbulence and approximately 40% chord at baseline conditions (see Figure 3.14). The current work's results seem to compare favorably with the predictions of the MISES solver in Figure 3.15 (Schreiber,2000). However, the MISES solver in Figure 3.20 predicts bypass transition at high Reynolds numbers and all turbulent intensities, while Figure 3.15-3.16 show that transition occurs inside of laminar separation bubble rather than in a bypass mode. Schreiber documents a similar experimental result trend to that of the current work, in that turbulent intensities as high as 2.5% and Reynolds number of $0.9x10^6$, transition still occurred within a laminar separation bubble. Even though the Schreiber saw the extent of the laminar separation decrease, or shorten, with increasing turbulent intensities the bubble could not be observed to disappear until the Reynolds number was raised to $2.2x10^6$, and turbulence intensity increased to 2.5%. At this Reynolds number a laminar separation bubble remained at turbulent intensities less than 2.5%. Schreiber went on to find that a turbulence intensity of 4%-5% was needed to make the bypass transition propagate upstream to about 6%-7% chord. In the current work it is realistic to assume that transition propagation did not occur due to the low turbulent intensity level; however, it is also realistic to conclude that the extent of the laminar separation was shortened.

Chapter 4 CONCLUSIONS AND RECOMMENDATIONS

Surface flow visualization and aerodynamic measurements were performed in an increased turbulent free-stream to document the effects of turbulence on the performance of a high turning compressor cascade at varying cascade incidence and inlet Mach number. The free-stream turbulence was increased from an intensity of 0.1% at baseline conditions, to a level of 1.3-1.6%. Blade surface static pressures and flow visualization were obtained and the total pressure loss coefficient was calculated for both experimental cases.

At negative cascade angles and an inlet Mach number range of 0.60-0.75, the total pressure loss coefficient was found to be reduced only negligibly with and without increased free-stream turbulence. This is due to the boundary layer remaining completely attached at the trailing edge of the blade under both conditions. At a slightly higher inlet Mach number, the cascade is found to approach the "choked" condition at negative cascade angles, leading to higher losses. The effects of free stream turbulence at this condition were found to be slightly adverse, due to the increased boundary layer thickness with increased free-stream turbulence.

At the lowest loss cascade angle and positive cascade angles, the effects of increasing free-stream turbulence on the pressure loss coefficient proved to be very significant. Losses were reduced by as much as 56% depending on the cascade angle and inlet Mach number. This loss reduction is seen to decrease with increasing inlet Mach number as the boundary layer approaches a completely separated condition on the suction surface. From the supersonic Mach

number maximum in the isentropic Mach number distribution, it was concluded that a shock wave exists on the suction surface for some cascade angles and inlet Mach numbers. The strength of the shock system within the passage determines the effectiveness of increased free-stream turbulence on the loss coefficient. Oil Visualization was performed for two cascade angles that were found to have a supersonic peak on their suction side Mach number distributions. For one angle, the boundary layer was found to be completely separated after boundary layer transition, which existed within a laminar separation bubble. At this condition the effects of free stream turbulence on the loss coefficient were found to be adverse. Again, due to tendency of increased free-stream turbulence to cause the boundary layer to thicken near separation. For the second angle, boundary layer transition was again found to exist within a laminar separation bubble, which was shortened by the effects of turbulence. In this case the boundary layer was found to reattach as a turbulent layer and then separate turbulently near the trailing edge of the stator. The pressure loss coefficient in this case was reduced by 11%. In conclusion, increased free-stream turbulence is an effective mechanism for the improvement of aerodynamic efficiency.

Research in this area has been greatly enhanced over the years; however, there is plenty of room for further research especially the in area of wake-induced transition and the role that surface roughness plays on this transition. The effects of a controlled AVDR on the loss coefficient at varying turbulent intensities at transonic inlet Mach numbers would be a “next-step” for the current work. A variation in turbulence length scale on the loss coefficient would also be in the interest of the progression of future work.

REFERENCES

Baines, WD. and Peterson, EG. "An Investigation of Flow Through Screens." Transactions of the ASME. July(1951): 467-480.

Carter, CJ. "Aerodynamic Performance of a Flow Controlled Compressor Stator Using an Imbedded Injector Pump." Thesis, Virginia Polytechnic Institute and State University, 2001.

Citavy, J. and Norbury, JF. "The Effect or Reynolds Number and Turbulence Intensity on the Performance of a Compressor Cascade with Prescribed Velocity Distribution." Journal of Mechanical Engineering Science. 19-3(1977): 93-100.

Evans, BJ. "Effects of Free-Stream Turbulence on Blade Performance in a Compressor Cascade." Dissertation, Cambridge University, CUED/A-Turbo/TR26, 1971.

Evans, RL. "The Effects of Freestream Turbulence on the Profile Boundary Layer and Losses in a Compressor Cascade." International Journal of Turbo and Jet Engines. 2(1985): 107-113.

Gostelow, JP. Cascade Aerodynamics. New York: Pergamon Press, 1984.

Holmberg, DG. "A Frequency Domain Analysis of Surface heat Transfer/Free-Stream Turbulence Interactions in a Transonic Turbine Cascade." Dissertation, Virginia Polytechnic and State University, 1996.

Kiock, R. "Influence of the Degree of Turbulence on the Aerodynamic Coefficients of Cascades." AGARDograph. 164(1972): 73-88.

Mayle, RE. "The Role of Laminar-Turbulent Transition in Gas Turbine Engines." ASME Journal of Turbomachinery 113(1991): 509-537.

Roach, PE. "The Generation of Nearly Isotropic Turbulence by Means of Grids." International Journal of Heat and Fluid Flow. 18-2(1987): 82.

Sauer, J. "The SUDI Generator-A Method to Generate High Freestream Turbulence Levels and a Range of Length Scales." Dissertation, University of Wisconsin, 1996.

Schetz, J. Boundary Layer Analysis. New Jersey: Prentice-Hall, 1993.

Schreiber, HA, et al. "Effects of Reynolds Number and Free-Stream Turbulence on Boundary Layer Transition in a Compressor Cascade." Proceedings of ASME Turbo Expo. Munich, Germany, 2000.

Steinert, W. and Starken, H. "Off-Design Transition and Separation Behaviour of a CDA Cascade." ASME Journal of Turbomachinery. 118-2(1996): 204-210.

APPENDIX A UNCERTAINITY ANALYSIS

The following is an uncertainty analysis of the major parameters and variables measured and used throughout this research. Inaccuracies due to bias and precisions errors compound in the calculations of certain parameters. Bias errors are present in all of the instrumentation or recording equipment used for this experiment, and was minimized wherever possible. Table A.1 summarizes the bias errors encountered during this research. Listed is the measured parameter, the instrument or calibrator used, along with the respective device's uncertainty range. Precision errors are found in the repeatability of the wind tunnel experiments, and are not included in the uncertainty analysis of the key parameters. Tunnel conditions were held within the operating capabilities of the transonic blow-down wind tunnel. The primary variable used to assess wind tunnel test repeatability was inlet Mach number. For all tests, a range of ±0.01 in the desired Mach number was accepted. If the Mach number did not fall within the desired range for a given test, the data was not accepted and the test was repeated. Quantization error due to the A/D converter of the data acquisition was negligible compared to the bias errors of the instrumentation and was neglected.

Measurement(s)	Instrument	Instrument Uncertainty
P_{S1}, dP_T, P_{S2}	Pressure Transducer 0-5.0 psid	+/- 0.025 psi
$P_{T1,PT2}$	Pressure Transducer 0-15.0 psid	+/- 0.075 psi
P_{amb}	Kahlsico Precision Aneroid Barometer MK2	+/- 0.002 psi
HW-Voltage	Dantec HW	+/- 2%
T_{T1}	Type K Thermocouple	+/- 2 K
Pitch	Probe Setup	+/-.05 in or 2.78%
Pitch	Traverse Mechanism	+/-.0162 in. or 0.9%
Incidence Angle	Digital Protractor	+/- 0.05 deg
Transducer Calibration	Fluke 0-30psi Calibrator	+/- 0.015 psi

Table A. 1: Bias Errors Due to Instrumentation and Uncertainty.

As key parameters were calculated using the data measured through instrumentation listed in Table A.1 errors compounded and propagated. The primary parameter of interest throughout this experiment was the area averaged total pressure loss coefficient, ω. The loss coefficient is found in its discrete form by using Equation 2.5 and its uncertainty is found as follows.

Equation A. 1
$$\delta\omega = \sqrt{\left[\left(\frac{\partial\omega}{\partial\Delta P_T}\right)\delta\Delta P_T\right]^2 + \left[\left(\frac{\partial\omega}{\partial P_{T1}}\right)\delta P_{T1}\right]^2 + \left[\left(\frac{\partial\omega}{\partial P_1}\right)\delta P_1\right]^2}$$

Total pressure loss coefficient is represented in Chapter 3 by the use of error bars.
Uncertainty of the inlet Mach number from Equation 2.6.

Equation A. 2
$$\delta M = \sqrt{\left[\left(\frac{\partial M}{\partial P_{T1}}\right)\delta P_{T1}\right]^2 + \left[\left(\frac{\partial M}{\partial P_1}\right)\delta P_1\right]^2}$$

The same method was used to identify the uncertainty of the isentropic Mach number, turbulent intensity, and AVDR, their values summarized in Table A.2. The uncertainty values appearing below represent the *maximum* errors encountered during experimentation, therefore the actually error for a given parameter may be less than stated in Table A.2. The AVDR uncertainty is considerably high due to the lack of a suitable downstream flow angle probe. This angle is estimated. The turbulent intensity calculation's uncertainty was done by Holmberg(1996).

Calculated Parameter	Maximum Propagated Uncertainty
Loss Coeff, w	+/- .008 or +/- 0.8%
Inlet Mach, M_1	+/- 0.011
Isentropic Mach, Ms	+/- 0.011
Tu	+/- 2.0% of value
AVDR	+/- 10% of value

Table A. 2: Maximum Propagated Uncertainty.

APPENDIX B DOWNSTREAM LOSSES AND M2 VS PITCH

The following plots, are examples of the wake profiles for a given testing condition. It should be noted that periodicity is somewhat of an issue due to lack of an effective tailboard to guide the exit flow through the exhaust of the test section. Most recent work from other researchers at Virginia Tech is addressing this problem and a first design iteration of a tailboard is being tested.

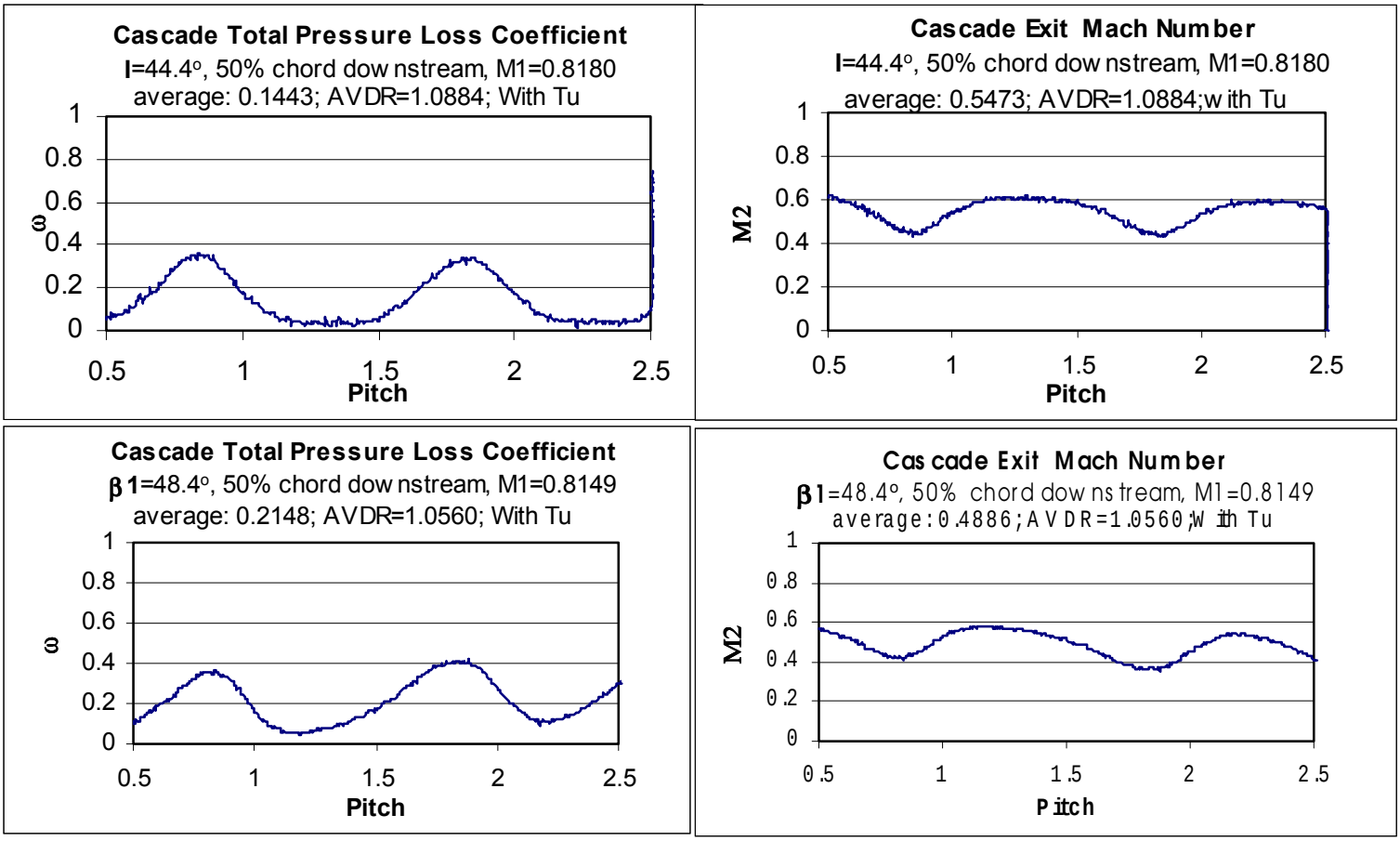

Figure B. 1: Sample of Downstream Loss and M2 Profiles

From Figure B.1, periodicity seems to worsen with increased cascade angle, this issue prompted the current design and fabrication of a tailboard to correct this problem. Further tunnel

modifications include: upstream sidewall suction and in passage sidewall suction, this will not only make the incoming flow realistic provide a means of control for AVDR.

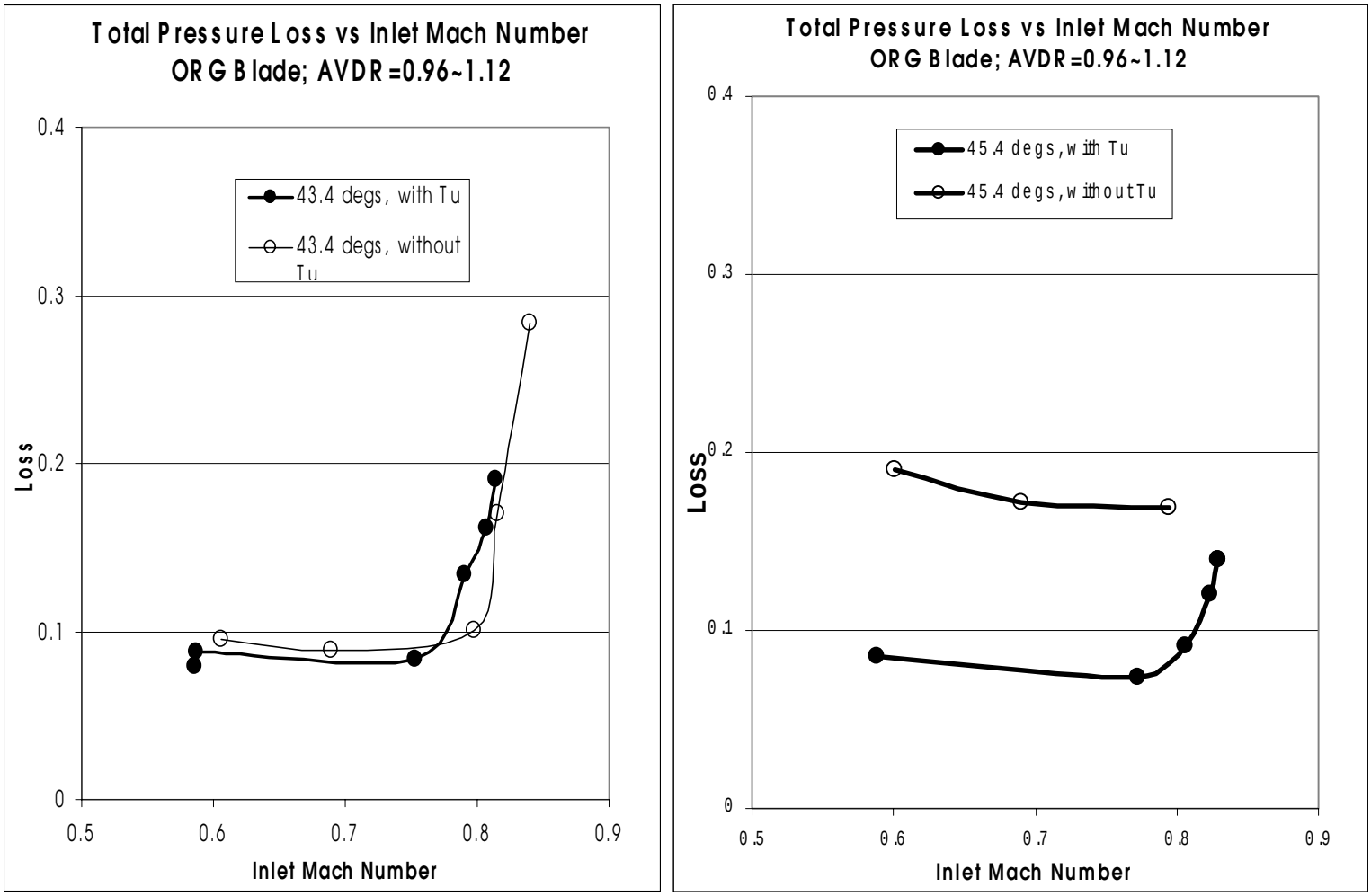

Figure B. 2 Loss vs Inlet Mach Number

APPENDIX C HOT WIRE CALIBRATION AND REDUCTION CODE

The following excerpt is taken from Holmberg(1996) and describes the one–point calibration theory for calculating velocities from the voltage fluctuations measured by the Hot Wire Probe.

Hot-wire calibration theory

The usual approach to calibrating a hot-wire is to place a hot-wire in a known velocity laminar jet and to record voltage out for a given flow velocity and temperature. The data is then used in an equation of this form:

$Nu = A + B\,Re^{x}$

The actual values for A, B, and x will vary some, but both Bradshaw (p. 115) and Hinze (2nd ed. p.89) give these numbers as applicable to the different Re_d regimes:

$$Nu\left(\frac{T_m}{T_s}\right)^{-0.17} = 0.24 + 0.56\,Re^{0.45} \qquad \text{for } Re_d < 44 \qquad (3.4)$$

$$Nu\left(\frac{T_m}{T_s}\right)^{-0.17} = 0.48\,Re^{0.51} \qquad \text{for } Re_d > 44 \qquad (3.5)$$

where the term T_m/T_s is a temperature correction factor, and the value of $Re_d = 44$ is where laminar to turbulent transition of flow over the wire occurs.

At wire transition the calibration curve shifts, as seen by the changed Reynolds number exponent (Re exponent), and the calibration curve also goes through the origin for higher Re. For typical cold conditions in the cascade tunnel (grid tests were done in unheated flow):

$M_{inlet} = 0.36$
$P_t = 31.7\text{psia} = 219\text{ kPa}$
$T_t = 290\text{K}$
$\gamma = 1.4$
$T_{wire} = 500\text{K}$
$d_{wire} = 5\mu\text{m}$
$R_{air} = 287\text{m}^2/\text{s}^2\text{K}$

$$\frac{P_t}{P_s} = \left(1 + \frac{\gamma - 1}{2}M^2\right)^{\frac{\gamma}{\gamma-1}} = \left(\frac{T_t}{T_s}\right)^{\frac{\gamma}{\gamma-1}}$$

which gives:

$P_s / P_t = 0.914$
$T_s / T_t = 0.975$
$T_s = 280$ K
$P_s = 29.0$ psia = 200. kPa

then:

$$T_m = \left(T_s + T_w\right)/2 = 390 \text{ (K)}$$

$$\rho_m = \frac{P_s}{RT_m} = 1.79 \quad (\text{kg/m}^3)$$

$$\mu_m = 1.716x10^{-5} * \left(\frac{T_m}{273.16}\right)^{1.5} * \left(\frac{383.716}{T_m + 110.556}\right) = 22.6\ x10^{-6} \quad (\text{Ns/m}^2)$$

$$U = \text{M}\sqrt{\gamma\ R_{air}\ T_s} = 121 \quad (\text{m/s})$$

$$\text{Re}_d = \frac{\rho_m U\, d_{wire}}{\mu_m} = 48$$

Therefore, the wire is actually operating near its transition point, but presumably in the turbulent regime. Two assumptions were made initially:

1) Re exponent = 0.51 can be applied to the grid turbulence measurements.

2) The calibration will be a straight line through the origin if plotted as:

$\text{Nu} = \text{const}*\text{Re}^{0.51}$

The above assumptions were tested experimentally and were found to be valid within the uncertainty of measurements. A discussion of the validity of these assumptions is included in the next section.

The result of the above two assumptions is that a calibration of a given wire can be obtained with data at only one point (where the origin becomes the second point). Calibration of the UHW used for performing grid turbulence field measurements was done *in-situ* with a calibration performed for each tunnel run using this method. This allowed a calibration without the uncertainty of a varying tunnel total temperature and pressure and changes in the wire itself from run to run. The specifics of this method follow.

One point calibration methodology

As discussed above, the conditions in the tunnel for measurements behind the grids upstream of the cascade allow for the use of this equation:

$$Nu\left(\frac{T_m}{T_s}\right)^{-0.17} = 0.48\,\text{Re}^{0.51} \qquad (3.5)$$

Now, each piece of this equation needs to be put into known measured quantities, and put into a form that can lead to a useful calibration.

$$\text{Nu} = \frac{hd}{k_m}, \quad \text{where} \quad h = \frac{(power)}{(area)(\Delta T)} = \frac{\left(\dfrac{V^2 R_w}{\left(R_w + R_1\right)^2} \right)}{\left(\pi\, d_w L_w\right)\left(T_w - T_s\right)}$$

where the above equation for the heat transfer coefficient is taken from Freymuth and Fingerson (1980). In this equation, HW voltage *V* and the tunnel static temperature T_s are the only variables. All wire properties are considered constant given a constant temperature anemometer that in theory maintains wire temperature and thus resistances constant. Therefore the equation for Nu reduces to:

$$\text{Nu} \propto \frac{V^2}{\left(T_w - T_s\right)k_m} \propto \frac{V^2}{\left(T_m - T_s\right)k_m} \quad \text{since } \left(T_w - T_s\right) = 2\left(T_m - T_s\right)$$

Then, taking the constant wire diameter out of Re, flipping the left and right hand sides of the equation for convenience, and inserting a calibration constant:

$$\left(\frac{\rho_m U}{\mu_m} \right)^{0.51} = C \frac{V^2}{\left(T_m - T_s\right)k_m} \left(\frac{T_m}{T_s} \right)^{-0.17} \tag{3.6}$$

simplified to:

$$\text{Re}' = C\,\text{Nu}' \tag{3.7}$$

This equation was used in the calibration of the UHW used for grid measurements. The specific step-by-step procedure of applying these equations follows.

1. Find the average Pt, Tt, and V (HW voltage) over the selected HW sample.
2. Solve for Ts, Ps, and Tm from the above equations using γ = 1.4 as the initial value.
3. Proceed through the following equations:

$$Cp_{air} = 1037.8 - 0.22371T_s + 2.8556x10^{-4}\,T_s^{\,2} + 5.2694x10^{-7}\,T_s^{\,3} - 5.3327x10^{-10}\,T_s^{\,4} \quad (\text{m}^2/\text{s}^2\text{K})$$

$$\gamma = \left(1 - \frac{\text{R}}{\text{Cp}_{\text{air}}} \right)^{-1}$$

$$P_s = P_t\left(1 + \frac{\gamma - 1}{2} M^2 \right)^{\frac{\gamma}{1-\gamma}} \quad (\text{Pa})$$

$$T_s = T_t - \frac{U^2}{2Cp} \quad (\text{K})$$

$$U = M\sqrt{\gamma\, R\, T_s} \quad (\text{m/s})$$

$$T_m = \left(T_s + T_w\right)/2 \quad (\text{K})$$

$$\rho_m = \frac{P_s}{RT_m} \quad (\text{kg/m}^3)$$

$$\mu_m = 1.716x10^{-5}\left(\frac{T_m}{273.16}\right)^{1.5}\left(\frac{383.716}{T_m + 110.556}\right) \quad (\text{Ns/m}^2)$$

$$k_m = 2.414x10^{-2}\left(\frac{T_m}{273.16}\right)^{1.5}\left(\frac{473.16}{T_m + 200}\right) \quad (\text{W/mK})$$

$$\text{Re}' = \left(\frac{\rho_m U}{\mu_m}\right)^{0.51}$$

$$\text{Nu}' = \frac{\left(\overline{V}\right)^2}{k_m\left(T_m - T_s\right)}\left(\frac{T_m}{T_s}\right)^{-0.17}$$

$$C = \text{Re}' / \text{Nu}'$$

This constant then can be used for all the HW data acquired in that run to convert bridge voltage to a velocity series. The value of C is for a given hot-wire, and will be consistent run to run with some small drift over time.

When using this calibration to solve for the velocity, the values of Re′ and Nu′ must be solved iteratively at each point. The progression is similar to the above calibration equations, but the result is U instead of a calibration constant. The method used was:

1) Solve for C_p, T_s, T_m, k_m, μ, γ as above.

2) Solve for Mach number, M.

3) Then Ps = f(P_t, γ, M).

4) Solve for Nu′ using the instantaneous HW voltage.

5) $(\rho U) = \mu(C^*\text{Nu}')^{1/0.51}$, where Re′ = C*Nu′

6) Mean density from the low speed data, $\rho_m = P_{s,m}/RT_s$

7) and then instantaneous $U = (\rho U)/\rho_m$ if density fluctuations are assumed negligible.

8) Iterate the above sequence until U converges.

The following is the Fortran Code used in the current work to generate velocities from the voltage fluctuations measured by the HW.

```
      program main
      real mach,nusselt
   OPEN(9,file='c:\temp\output.txt')
      OPEN(7,file='c:\temp\check.out')
      OPEN(5,file='c:\temp\hotfilm.txt')
      OPEN(6,file='c:\temp\labview.txt')

      r20=3.46
      arfa20=0.36
      rop=6.78
      offset=7.0
      gain=1.0

      tw=(rop-r20)/arfa20*100./r20+20.
      tw=tw+273.15
      dw=5./1000./1000.
      tol=0.005
c*****************************************************************************************
      read(5,*) number
      read(5,*) vhotavg
      write(9,30) number,vhotavg
30    format(/'number=',i7,' vhotavg=',f12.4)
      vhotavg=vhotavg/gain+offset
      read(6,*) pt
      read(6,*) tt
   read(6,*) ps
      read(6,*) patm
      write(7,40)       pt,tt,ps,patm
40    format('Pt= ',f10.4,'psig ','Tt= ',f10.2,' c  Ps=',f10.4,
     1                  'psig  Patm=',f10.1,'Pa')
      close(7)
c*****************************************************************************************
      pt=pt*6894.8+patm
      ps=ps*6894.8+patm
      tt=tt+273.15
      mach=sqrt(5.*((pt/ps)**(1/3.5)-1))
      ts0=tt/(1.0+0.2*mach*mach)
      velocity=mach*sqrt(1.4*287.0*ts0)
      tm0=(ts0+tw)/2
      dens0=ps/287/tm0
      visty0=1.716/100000.*(tm0/273.15)**1.5*383.716/(tm0+110.6)
      cond0=2.414/100.*(tm0/273.15)**1.5*473.16/(tm0+200.)
      reynolds=(dens0*dw*velocity/visty0)**0.51
      nusselt=vhotavg**2/cond0/(tm0-ts0)*(tm0/ts0)**(-0.17)
      constant=reynolds/nusselt
      do 1000 i=1,number
      read(5,*)         hotfilm
      hotfilm=hotfilm/gain+offset
      icount = 0
   temp=constant*hotfilm**2/(tm0-ts0)/cond0*(tm0/ts0)**(-0.17)
      utemp=temp**(1/0.51)/dens0/dw*visty0
```

```
100       ts=tt-utemp**2/2/1005.
          sound=sqrt(1.4*287.0*ts)
          mach=utemp/sound
    tm=(ts+tw)/2
          dens=ps/287/tm
          visty=1.716/100000.*(tm/273.15)**1.5*383.716/(tm+110.6)
          cond=2.414/100.*(tm/273.15)**1.5*473.16/(tm+200)
          nusselt=constant*hotfilm**2/cond/(tm-ts)*(tm/ts)**(-0.17)
          utemp1=nusselt**(1/0.51)/dens/dw*visty
          ut=(utemp+utemp1)/2.
          if(abs(ut-utemp1).le.tol) goto 900
          utemp=ut
          icount=icount+1
          if(icount.ge.10000) goto 500
          goto 100
500       write(9,600) i, icount
600       format(//'i= ', i7,' icount=',i6,' error happen')
900       hotfilm=(hotfilm-offset)*gain
          write(9,950) hotfilm,ut
950   format(f12.4,',',f12.4)
1000      continue
          close(5)
          close(6)
          close(9)
          stop
          end
```

This code was written by Shiming Li and the author, it is based on the code from Holmberg(1996).

APPENDIX D REDUCTION CODE FOR TURBULENCE SCALE

```
% Matlab M-file to reduce Hotwire Data and Perform Spectral Analysis:

% Data taken on 01/27/01 using LeCroy and Labview:
% LeCroy Data were sampled at 20 kHz (dt=50 us), DC offset -5V, filtered at
10kHz, 2 V FSV
% Location 3:

clear all; close all;

%Lecroy:
fsample=50000; % Sampling frequency of 50 kHz
dt=1/fsample; % Sampling period (sec)
N=8189; %Number of Samples 512Kx128K
T=N*dt; %Total Sampling Period (seconds)
df=1/T; %Frequency Resolution
t=[0:dt:T]; %Define time T=(Number Samples)*(dt), dt=1/(Sampling Frequency)
f=[0:df:fsample]; %Define frequency range from 0 to fsample in increments of
df

%Read in LeCroy data files and reduce data:
load vel3.txt;
hwv1=vel3(:,1); %Read first column and add back on 5 V DC component
hwv2=vel3(:,2);
hwv3=vel3(:,3);
Vmean(1)=mean(hwv1);
Vmean(2)=mean(hwv2);
Vmean(3)=mean(hwv3);

%PART a): DETERMINE STATISTICS:
%_____________________________________________________________________________
_________________

%Fluctuating component (a):
v1=hwv1-Vmean(1);
v2=hwv2-Vmean(2);
v3=hwv3-Vmean(3);

RMS1=(mean(v1.^2)).^0.5;
RMS2=(mean(v2.^2)).^0.5;
RMS3=(mean(v3.^2)).^0.5;

%PART b): PLOT AUTOCORRELATION CURVE AND DETERMINE INTEGRAL LENGTH SCALE:
%_____________________________________________________________________________
_________________

%Calculate autocorrelation on each data file:
Rv1=xcorr(v1,'coeff');
Rv1=Rv1(8190:16379);
Rv2=xcorr(v2,'coeff');
Rv2=Rv2(8190:16379);
Rv3=xcorr(v3,'coeff');
Rv3=Rv3(8190:16379);
```

```
%Plot autocorrelations:
figure(2);
plot(t,Rv1,'k',t,Rv2,'b',t,Rv3,'r');
xlabel('\tau (s)'); ylabel('Rv(\tau)');
title('Figure 1: Autocorrelation');
legend('Set 1','Set 2','Set 3');
grid on;
axis([0 0.0005 -0.2 1.2]);

%Perform Numerical Integration to Calculate Integral Time Scale:
%Complete Data Set:  First zero crossing calculated with find command:
z1=find(abs(Rv1)<0.002&abs(Rv1)>=0);
T1=sum(Rv1(1:z1(1)))*dt; %T is integral time scale
L(1)=T1*Vmean(1);

z2=find(abs(Rv2)<0.002&abs(Rv2)>=0);
T2=sum(Rv2(1:z2(1)))*dt; %T is integral time scale
L(2)=T2*Vmean(2);

z3=find(abs(Rv3)<0.002&abs(Rv3)>=0);
T3=sum(Rv3(1:z3(1)))*dt; %T is integral time scale
L(3)=T3*Vmean(3);
```

This code was written by Andrew Nix, graduate student at Virginia Tech.

VITA

Justin W. Douglas

Justin Douglas was born in Charleston, West Virginia on July 27, 1977. He graduated with distinction from the Virginia Military Institute in Lexington, Virginia with a Bachelor of Science degree in Mechanical Engineering in May of 1999. In addition to an outstanding undergraduate academic record, he was a three year letterman in Division I football. He published his first paper in an American Society of Engineering Education Journal in his final year at VMI. He studied abroad at St. Catherine's College, Oxford University in his third year at VMI. He was a semi-finalist for the Rhodes Scholarship in the state of West Virginia in 1998. Upon the completion of his undergraduate study he began his graduate studies at Virginia Tech under the guidance of Dr. Wing Fai Ng. The author defended his work on March 1, 2001. Upon graduation, the author began work at Ford Motor Company.